Monitoring Protein Conformations
and
DNA-Protein Interactions
via
Single Molecule-FRET Measurements

Masterarbeit aus dem Fachgebiet
Physikalische Chemie
von

BSc. Martina Preiner
geboren am 6. Juni 1985
in Burghausen

für die Masterhauptprüfung in Chemie an der
Ludwig-Maximilians-Universität

Datum der mündlichen Prüfung:	23. April 2009
Beginn der Masterarbeit:	18. Mai 2009
Masterarbeit beim Prüfungsausschuss eingereicht am:	27. November 2009

ERKLÄRUNG

Ich versichere hiermit, dass sich die vorgelegte Masterarbeit am Department Physikalische Chemie der Ludwig-Maximilians-Universität München, unter der Anregung von Prof. Don C. Lamb, PhD, selbständig durchgeführt und keine anderen als die angegebenen Hilfsmittel und Quellen benutzt habe.

München, den 27. November 2009

_____

Erstgutachter: Prof. Don C. Lamb, PhD

Zweitgutachter: Prof. Dr. Christoph Bräuchle

Wer am Ende ist, kann von vorn anfangen,
denn das Ende ist der Anfang von der anderen Seite.

Karl Valentin

Jeder Mensch macht Fehler.
Das Kunststück liegt darin, sie dann zu machen, wenn keiner zuschaut.

Sir Peter Ustinov

Eine Semmel enthält 140 Kalorien, 700 Semmeln pro Jahr ergeben 98000 Kalorien.
Diese benötigt man, um eigenhändig 1 Elefanten 9 Zentimeter weit zu tragen.
Aber wozu?

Loriot

ABSTRACT

Observing concrete steps and dynamics of biochemical processes is nowadays an important tool to discover the secrets of life. In many cases, fluorescence microscopy and spectroscopy on single molecules enable these kinds of investigations. Measurements on single molecules are highly facilitated by confocal fluorescence spectroscopy. By combining single molecule measurements with Förster resonance energy transfer (FRET), snapshots of the distribution of conformational states of a biomolecule are accessible. The general expression for this combination of single molecule measurements and FRET is termed single-pair FRET (spFRET). This technique can be used to monitor the major maintenance processes of all life forms: transcription and translation of the genetic information. During transcription, the information encoded in the genetic storage – the DNA (deoxyribonucleic acid) molecules – is copied by an assembly of proteins. The transcript of this process is called mRNA (message ribonucleic acid). The TATA box binding protein (TBP) is the first protein in the transcriptional process which binds to DNA at a certain site – the TATA box – and initiates the recruitment of further transcription factors. Eventually, the protein which conducts the actual transcription, RNA polymerase, binds to the complex and transcription begins. Recently there have been made great efforts to monitor the dynamics of DNA transcription and of protein-DNA interactions in general. In this study, in order to obtain a three-dimensional view of this interaction a precursor for investigation of DNA dynamics induced by TBP was designed. Thereby it was important to ensure proper binding of TBP to the TATA box on the DNA construct. This could be assayed by determine the diffusion time of TBP before and after binding to DNA by fluorescence correlation spectroscopy (FCS) and fluorescence cross-correlation spectroscopy (FCCS).

The product of transcription, mRNA, needs to be translated in a polypeptide which then folds into a native protein. Some polypeptides need support from other proteins, so-called chaperones, to fold properly. A very well studied chaperone system is the chaperonin complex GroEL/GroES. Still, the mechanisms of GroEL/GroES-mediated protein folding are not yet completely understood as the single steps of the folding cycle are not fully characterized. In this study, the question is addressed, in how far the initial binding of polypeptide substrates to the GroEL/ES chaperonin system subunit GroEL is relevant for the rest of the GroEL/ES activity cycle. Therefore, spFRET measurements with single ring mutants of GroEL were conducted that show a different substrate binding behavior.

I Introduction 1

I.1 How we got here 1
I.2 Aims of this Thesis 5

II Fluorescence Spectroscopy 6

II.1 Basic Principles of Fluorescence 6
II.2 Confocal Fluorescence Spectroscopy 9
II.3 Förster Resonance Energy Transfer (FRET) 10

III Analysis Methods 14

III.1 Multiparameter Setup 14
III.2 Setup Adjustments 16

III.2.1 Calculation of the Green and Red Confocal Volume 16
III.2.2 Determination of the γ-Factor 17

III.3 Fluorescence Correlation Spectroscopy (FCS) 18
III.4 Burst Analysis 20
III.5 Pulsed Interleaved Excitation (PIE) 21

IV Materials and Chemical Methods 25

IV.1 Stocks and Solutions 25

IV.1.1 Protein- and DNA Tile-Stocks 25
IV.1.2 Buffers 27

IV.2 Polyacrylamide and Agarose Gel Electrophoresis 28
IV.3 DNA-Gel-Extraction 29
IV.4 Ethanol Precipitation 30

V Exploring the GroEL/ES Chaperonin System 31

V.1 MBP as a Substrate of the GroEL/GroES-System 34
V.2 Initial Binding of DM-MBP to GroEL and its Mutants 36
V.3 Discussion 43
V.4 Construction of a Coaxial Mixer 44

VI Monitoring Protein-DNA Interaction 47

VI.1 The TATA Box and Its Binding Protein 47
VI.2 DNA-Constructs Beyond the Double-Helix 49
VI.3 Observing TBP-DNA Binding Using FCS 52

VI.3.1 Autocorrelation Functions 52
VI.3.2 Cross-correlation Functions 59

VI.5 Discussion 63

VI.5.1 Self-Assembly of a DNA Double Triple Crossover (DTX) Complex 63
VI.5.2 Binding of yTBP to a DNA-DTX Complex 63

VII Summary and Outlook 65

VII.1 Single Ring-GroEL Mutants 65
VII.2 DNA-TBP Binding and Three-Color-PIE 66

VIII Abbreviations 68
IX References 69

I Introduction

I.1 How we got here

Biomolecules like proteins and DNA provide the basis of every single life form. During the previous century many far-reaching steps have been taken to understand how these compounds regulate cell maintenance. An important question has always been that of heredity. The first secret was disclosed in 1943 by Oswald Avery. After his unambiguous experiments with pathogenic and non-pathogenic bacteria strains a cell compound named deoxyribonucleic acid – DNA – was identified as the transforming **principle of inheritance** (1). The next big breakthrough came exactly ten years later with the solution of the actual **DNA structure** (2). James Watson and Francis Crick are not only the fathers of the double helix, but also were the pioneers of interdisciplinary natural scientific research. From there on, the three main branches of the natural sciences – chemistry, physics and biology – started to work closer together. The second half of the 20th century is full of resounding discoveries concerning the molecular activities in all kinds of living creatures.

Another important step towards contemporary research was already made in the 1960s, when the **Green Fluorescent Protein**, GFP, was purified from the jellyfish *Aequorea Victoria* and its properties studied carefully by Osamu Shimomura. After the first crystal structures of GFP were published (3), researchers got a vital background on chromophore formation of the fluorescent protein – the amino acid residue interactions which eventually result in fluorescence. Based on the observed chromophore, scientist modified these residues to produce a wide variety of GFP derivatives. From there on, proteins could easily be tagged with fluorescent labels.

Parallel to the biochemical research, the 20th century can gloat over a striking development in light microscopy. Around the turn of the century the first **fluorescence microscope** was constructed by the physicist Oskar Heimstädt (4). Although Heimstädt successfully imaged bacteria, he wasn't convinced that fluorescence microscopy would have a lasting impact.

In fact, the reliance on autofluorescence of the imaged object and the need for transmitted illumination and darkfield condensers limited the initial applications of the microscope. Both hurdles were overcome during the next two decades, when the Austrian investigator Max Haitinger together with other scientists developed the technique of **secondary fluorescence**, which involved applying exogenous fluorescent chemicals to samples. Haitinger also coined the term “fluorochrome”.

Fluorochromes were essential to the use of fluorescence microscopy on living tissue, as was the development of the incident light (epi)-fluorescence microscope. Here, the light source lies on the same side of the sample as the objective, and excitation and emission light pass through the objective. The prototype of the epi-fluorescence microscope was designed in 1929 by German pharmacologist Philipp Ellinger and anatomist August Hirt. Ellinger and Hirt imaged kidney and liver tissue in rodents injected with the fluorochromes fluorescein and trypaflavin (5).

Another major advance came almost 40 years later, with the invention of dichromatic (or dichroic) beamsplitters, or **dichromatic mirrors**. Instead of absorbing certain wavelengths, as traditional filters did, dichromatic filters reflect a narrow width of wavelengths while transmitting all others, allowing illumination of the sample with a precise wavelength and ensuring that photons from the light source are not transmitted to the ocular (6). Dichromatic mirrors converted the epi-fluorescence microscope from a tool that could be used only by trained specialists to a universal and indispensable instrument for modern biology.

During the 1960s, researchers worked to overcome a debilitating feature of epi-fluorescence microscopy – background signals. The result was the advent of **confocal microscopy** (7). The resolution achievable with conventional microscopy can be negated by out-of-focus information. Confocal microscopy avoids this issue by restricting both the field of illumination and the light reaching the objective to a single point in the same focal plane (see Figure 1).

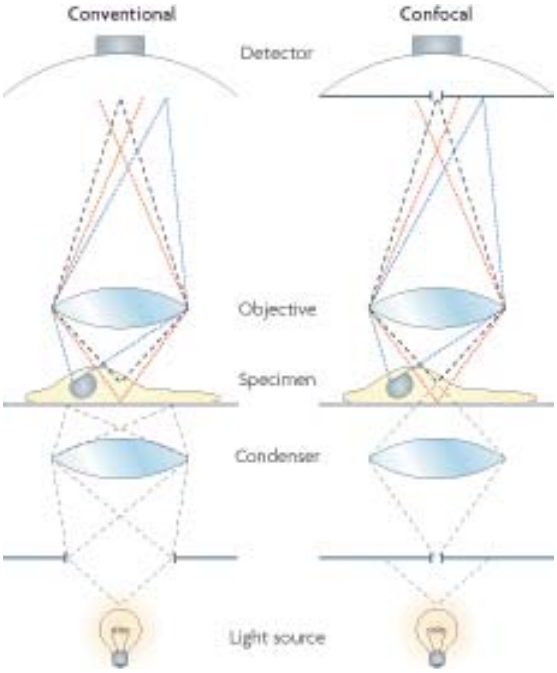

Figure 1 Optical path of a conventional microscope compared to a confocal microscope. Adapted from (8).

An image of the region of interest is then built up by raster scanning through the sample. Several follow-up studies made a key adjustment to the confocal design – the **use of laser beams**. This allowed faster scanning and higher resolution, but, most importantly, provided the illumination needed to obtain fluorescence images. Two papers published in 1987 used such instruments in the first key applications of confocal microscopy to cell biology (9, 10). In this way, the advantages of confocal microscopy for analyzing subcellular processes became clear. By revealing clear images in thick tissue samples, confocal microscopes obviated the need for tissue sectioning, and allowed tissues to be imaged under more physiological conditions. Together with the discovery of green fluorescent protein this ushered in the era of imaging in living cells.

The potential to visualize bright fluorescent molecules on a dark background provided molecular specificity and image contrast unparalleled by other dyes. Theory suggested that these properties should permit the **detection and imaging of single molecules**. Although the next two decades witnessed the detection of single fluorophores at low temperatures, or while transiting a highly focused laser beam, such methods were incapable of repeatedly imaging identified molecules in ambient environments. In 1993, this situation changed when the first repetitive imaging of single fluorophores at room temperature was reported (11). The potential biological applications of single-molecule imaging captured the imaginations of microscopists and biologists alike. In 1998, Sunney Xie and colleagues used the intrinsic on/off fluorescence switching of flavin adenine dinucleotide in the active site of cholesterol oxidase to reveal that enzyme activity is influenced by a form of molecular memory residing in conformational changes in the protein. This behavior was completely unanticipated from ensemble experiments (12). This showed unequivocally that **single-molecule microscopy** could shed new light on seemingly well-characterized systems.

Besides the developments in light microscopy and cell biology, one physical theory turned out to be essential for contemporary biochemical and biophysical research. The theory behind the so-called **Förster resonance energy transfer** (FRET) – also known as fluorescence resonance energy transfer – was first formally proposed in the 1940s by Theodor Förster (see also chapter II.3). He showed that electronic excitation energy can be transferred from a donor fluorophore to an acceptor chromophore in close proximity (13). Förster's proposal was confirmed experimentally in 1967 by Lubert Stryer and Richard Haugland, who demonstrated that the phenomenon of resonance energy transfer could be used as a “spectroscopic ruler” to determine the distance between two chromophores (14).

These findings paved the way for using FRET to observe interactions and conformational dynamics in purified proteins *in vitro*. FRET is suited to imaging protein-protein interactions in cells because the two fluorophores must be in very close proximity for FRET to be observed.

In combination with confocal fluorescence microscopy FRET techniques began to flourish (15). Since these landmark developments, the importance of FRET as a microscopy technique has been borne out in its application to challenging biological questions, such as the existence of lipid rafts (16). A wide variety of FRET-based biosensors are now available for detecting small molecules and enzyme activities in cells. And the technology continues to evolve, as novel donor-acceptor pairs are developed, new methods are introduced and instrumentation improves.

I.2 Aims of this Thesis

The work performed during this thesis ties in with single molecule-FRET measurements in protein folding and protein-DNA interaction. After a short introduction to the theory of fluorescence (chapter II) and the analysis methods (chapter III), the applied biochemical and technical methods are presented in chapter IV.

Chaperonin-assisted protein folding constitutes an important process in all living creatures. The GroEL/ES-chaperonin system e.g. enables faster renaturation of denaturized proteins like the maltose binding protein (MBP). Although GroEL/ES has been studied for more than a decade, there are still many unanswered questions about the process. The issue, whether the initial binding of MBP to the GroEL subunit is relevant for the ensuing folding procedure is subject of chapter V.

The motive of chapter VI is gaining a deeper insight in the dynamics of DNA-protein interactions. The chapter describes the synthesis of a DNA construct which provides three dimensional information of its own movements. Thus, any conformational change of the DNA could be monitored exactly.

II Fluorescence Spectroscopy

II.1 Basic Principles of Fluorescence

Fluorescence is an optical phenomenon in which the molecular absorption of a photon triggers the emission of a photon with a longer, i.e. less energetic, wavelength. The energy difference between the absorbed and emitted photons is converted into molecular rotations, vibrations or heat.

Excitation: $S_0 + h\nu_{ex} \rightarrow S_1$

Emission (fluorescence): $S_1 \rightarrow S_0 + h\nu_{em}$

S_0 *:* electronical ground state

S_1*:* first electronical excited state

$h\nu$ *:* generic term for photon energy

h *:* Planck's constant

$\nu_{ex/em}$: frequency of excitation and emission, respectively, dependent on the specific system

The more general term photoluminescence describes the process in which a substance absorbs photons (electromagnetic radiation) and then re-radiates photons. Quantum mechanically, this can be described as an excitation to a higher energy state and then a return to a lower energy state accompanied by the emission of a photon. Photoluminescence can be divided into fluorescence, delayed fluorescence and phosphorescence. The **Jablonski Diagram** (Figure 2) displays the relation between these three forms.

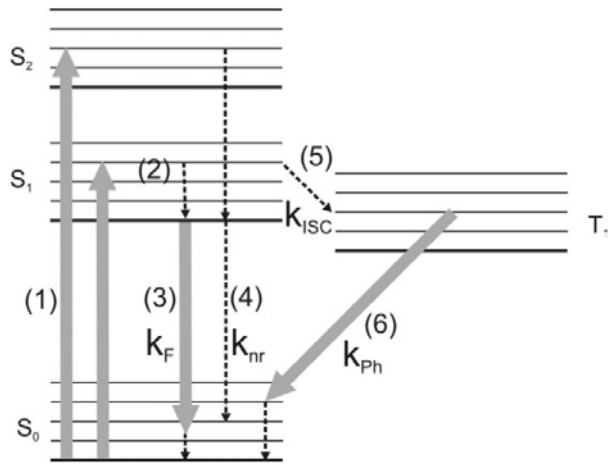

Figure 2 Jablonski Diagram: (1) absorption, (2) vibrational relaxation, (3) fluorescence, (4) internal conversion, (5) intersystem crossing, (6) phosphorescence. Taken from (17).

Before excitation, the electronic configuration of the molecule is described as being in the electrical ground state (S_0). Because of the instantaneous nature of light absorption (depicted as vertical lines in a Jablonski diagram), transitions last about 10 fs, which is too short for relevant nuclei displacement (Born-Oppenheimer approximation). This assumption constitutes the basis of the **Franck-Condon principle** for electronic transitions: When the electron moves to a new vibrational level during the electronic transition, this new vibrational level must be instantaneously compatible with the nuclear positions and momenta of the vibrational level of the molecule in the originating electronic state. Figure 3 illustrates the Franck-Condon principle.

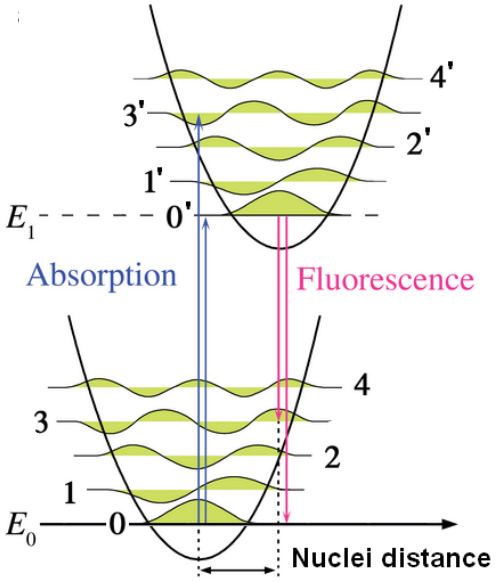

Figure 3 Visualization of the Franck-Condon principle. Taken from (18).

Hence, for excitation or also for de-excitation the Franck-Condon principle states, that after excitation the molecule is not in the vibrational ground state of the S_N-state, but in a higher vibrational level. The molecule will relax quickly to the lowest vibrational state and can then return to the ground state by various competing pathways. If that happens by spontaneous emission of a photon, this event is called fluorescence. In a non-radiative relaxation the excitation energy is dissipated as heat, i.e. vibrations, to the environment. Relaxation via conversion to a triplet state is also possible. This triplet state can subsequently relax via phosphorescence, by a secondary non-radiative relaxation step or by delayed fluorescence. Fluorescence quenching is another possibility to relax from a S_1 state e.g. by interaction with a second molecule without emission of a photon.

The fluorescence **quantum yield** is the ratio of the number of fluorescence photons emitted to the number of photons absorbed during excitation. It represents the amount of radiative and non-radiative decay and thus the efficiency of the fluorescence process. If every photon absorbed results in a photon emitted, the quantum yield is 1.0. Another way to define the quantum yield of fluorescence is by the rates of excited state decay:

$$\phi = \frac{k_f}{\sum_i k_i}$$

ϕ: quantum yield

k_f: rate of spontaneous emission of radiation

k_i: non-radiative decay processes

The other rates of excited state decay do not result in emission of a photon. They are often called non-radiative rates and include: dynamic collisional quenching, resonance energy transfer, internal conversion (transition between energy states of the same spin state) and intersystem crossing (transition between different spin states).

If the rate of any pathway changes, this will affect both the measured excited state lifetime and the fluorescence quantum yield. As the energy of the emitted photon is lower than that of the excitation photon, emission occurs at a longer wavelength than excitation. The difference in energy $h\nu_{ex} - h\nu_{em}$ is called the **Stokes' shift**. Due to the Stokes' shift, emission photons are detected at a different wavelength than excitation photons. Fluorescence microscopy allows the detection of even low levels of emitted light that originates from fluorescent probes like synthetic fluorescent dyes or expressed fluorescent proteins. Hence, it constitutes a popular method to observe the smallest objects and processes like biochemical pathways (17). There are many different fluorescence microscopy applications. Imaging is realized by wide-field and scanning fluorescence microscopy. In a widefield microscope, the entire specimen is bathed in light from a mercury or xenon source, and the image can be viewed directly by eye or projected onto an image capture device or photographic film. Scanning becomes necessary, if only one point of the sample is illuminated. The advantages of point illumination (and detection) will be described in the following chapter.

II.2 Confocal Fluorescence Spectroscopy

In contrast to a conventional wide-field fluorescence microscope, confocal microscopy uses point illumination and a pinhole in an optically conjugate plane in front of the detector to eliminate out-of-focus information (see Figure 4). Only the light within the focal plane is detected, so the axial resolution is much better than that of wide-field images. The diameter of the confocal volume is defined by the numerical aperture of the objective lens and by the optical properties of the sample and the ambient index of refraction.

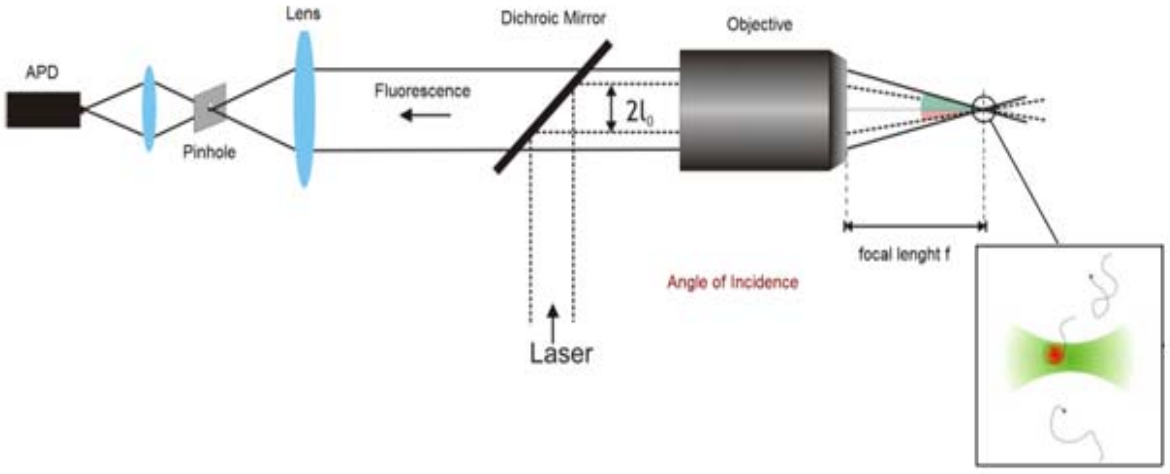

Figure 4 Schematic of the coupling of a confocal microscope with a laser excitation source. Adapted from (17).

The volume within a sample that is efficiently detected is called “the confocal volume”. The confocal volume is typically on the order of femtolitres or less and is often used to create the small detection volume required in fluorescence correlation spectroscopy (FCS) measurements (see III.1). As only one point is illuminated at a time in confocal microscopy, 2D or 3D imaging usually requires scanning, except for techniques like spinning disc microscopy.

II.3 Förster Resonance Energy Transfer (FRET)

Although confocal microscopy provides a high resolution compared to wide-field techniques, it is still bound to the optical diffraction limit. During the last decades large efforts were taken to beat the diffraction limit by various methods like e.g. stochastic optical reconstruction microscopy (STORM), photoactivated localization microscopy (PALM) and stimulated emission depletion microscopy (STED). All of these techniques provide improved transverse spatial resolution. But there are other possibilities to bypass the diffraction limit. One example is "Förster (or fluorescence) resonance energy transfer" (FRET), a phenomenon that can occur between two fluorescent dyes. FRET is a distance-dependent interaction between the electronic excited states of two dye molecules. It involves the radiationless transfer of energy from the excited state of a so-called donor fluorophore to the excited state of a neighbouring acceptor fluorophore by a dipole-dipole coupling mechanism.

The basic requirement for FRET is an overlap of the acceptor's absorption spectrum and the donor's fluorescence emission spectrum. Because the efficiency of energy transfer varies inversely with the sixth power of the distance separating the donor and acceptor fluorophore, energy can be transferred in this way only over small distances, effectively limiting FRET to a range of 2 to 10 nm (for distances < 2 nm, Dexter electron transfer occurs rather than FRET) (19). Furthermore, the donor and acceptor dipoles must be in a favourable orientation (20). The resonance energy transfer efficiency f_E is expressed by the means of following equation:

$$f_E = \frac{R_0^6}{R_0^6 + r^6} = \frac{1}{1 + \left(\frac{r}{R_0}\right)^6}$$

The Förster distance R_0 describes the distance r between two fluorophores at which the decay and energy transfer rates are equal.

$$R_0^6 = 8.8\ 10^{-28} \kappa^2 n^{-4} \phi_D J \text{ in } [\text{Å}^6]$$

κ^2: orientation factor

n: index of refraction of the solvent

ϕ_D: quantum yield of the donor in the absence of the acceptor

J: spectral overlap between the fluorescent emission of the donor and absorption of the acceptor

The orientation factor results from the dipole orientation as follows:

$$\kappa^2 = (\cos\theta_T - 3\cos\theta_D \cos\theta_A)^2$$

θ_T: angle between the donor and acceptor transition dipole moment

$\theta_{D/A}$: angles between the donor/ acceptor transition dipole moment and the line joining the fluorophores

The value of κ^2 can range from 0 to 4, depending upon the relative orientation of donor and acceptor (21). Figure 5 shows the general arrangement of the absorption and emission transition moments.

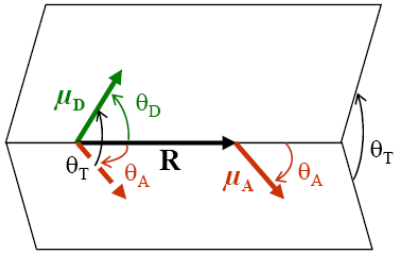

Figure 5 General dipole moment orientation of donor and acceptor in order to define κ^2. $\mu_{D/A}$ is the transition dipole moment of donor and acceptor, respectively. *R* is the distance between donor and acceptor.

Normally, an average value of 2/3 can be used for κ^2, which equals the value for donors and acceptors diffusing rapidly through all possible orientations over the time span of energy transfer (21).

The overlap integral *J* expresses the degree of spectral overlap between the donor emission and the acceptor absorption. It is calculated as:

$$J = \frac{\int F_D(\lambda)\varepsilon_A(\lambda)\lambda^4 d\lambda}{\int F_D(\lambda) d\lambda} = \int f_D(\lambda)\varepsilon_A(\lambda)\lambda^4 d\lambda \text{ in } [\mathrm{M^{-1}cm^3}]$$

F_D: Fluorescence intensity of the donor

ε_A: molar extinction coefficient of the acceptor

f_D : normalized emission spectrum of the donor

Although FRET has been used for many years as a molecular ruler (14, 22), it is the emergence of the fluorescent protein tags that has made FRET microscopy more generally applicable to biochemical and biomedical research. The efficiency of FRET from a donor to an acceptor can be improved by increasing the overlap of the donor emission spectra with the absorption spectra for the acceptor. The trade-off for this improved efficiency, however, is that there will be an increase in spectral crosstalk (23).

There are several possibilities to measure FRET efficiencies. In bulk measurements using a fluorescence spectrometer, information of the sample's heterogeneity gets lost because it averages over all FRET efficiencies. Besides, it is impossible to draw a conclusion about the labeling efficiency of the sample. Donor-only labeled molecules for example result in apparently high FRET efficiencies. Single molecule measurements avoid this ensemble averaging and thus provide information about sample heterogeneities and subpopulations.

In this thesis the burst approach is used in order to conduct single molecule measurements (see chapter III.4). Freely diffusing molecules pass the confocal excitation volume in a concentration low enough to ensure that the probability to have more than a single molecule at a time in the confocal volume is negligible (10 to 50 pM). During their way through the focus, a burst of photons is registered which can last up to several milliseconds. To detect FRET efficiencies, donor excitation is used and the fluorescence is detected in two channels: one detects the donor fluorescence, the other the acceptor fluorescence. A burst is included in the analysis when the sum of the arriving photons in a burst exceeds a given threshold in the detection channels.

The FRET efficiency f_E can be calculated based on the ratio of the fluorescence intensity of the acceptor in the donor's presence F_{AD} to the total fluorescence intensity (the sum of the acceptor and the donor intensity in each other's presence $F_{AD} + F_{DA}$).

$$f_E = \frac{F_{AD}}{F_{AD} + \gamma \cdot F_{DA}}$$

The correction factor γ is defined as the ratio of the products of donor and acceptor detection efficiency $\eta_{D/A}$ and quantum yield $\phi_{D/A}$, respectively. It can be determined experimentally, which is described in chapter III.2.2.

$$\gamma = \frac{\eta_A \cdot \phi_A}{\eta_D \cdot \phi_D}$$

For exact calculations of the FRET efficiency, two further correction terms have to be considered: spectral crosstalk of the donor in the acceptor channel and direct excitation of the acceptor by the donor excitation. Their values are determined for the utilized dye pair before starting the measurements, but still only a mean value can be included. That leads to occasional FRET efficiencies below 0 % or above 100 %. The following equation for the FRET efficiency f_E considers each correction term (17).

$$f_E = \frac{F_{AD} - F_A \cdot \beta_{dE} - F_{DA} \cdot \beta_{CT}}{F_{AD} - F_A \cdot \beta_{dE} - F_{DA} \cdot \beta_{CT} + \gamma \cdot F_{DA}}$$

β_{dE}: correction factor for direct excitation

β_{CT}: correction factor for spectral crosstalk

F_A: fluorescence intensity of all active acceptors

III Analysis Methods

III.1 Multiparameter Setup

During this work, a four-channel setup based on a Nikon TE300 (*Nikon*, Tokyo, Japan) inverted microscope was used. The system is mounted upon an optical table (*Melles Griot*, Albuquerque, USA). A schematic drawing of the optical and electrical paths is shown below.

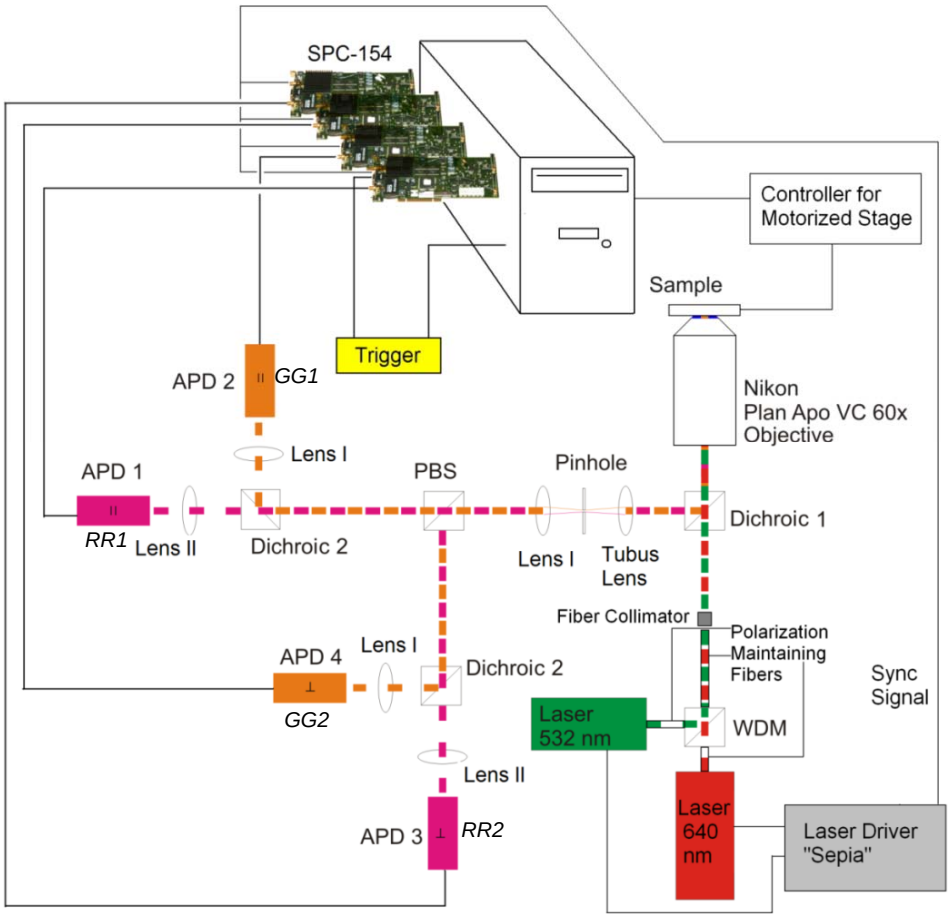

Figure 6 A schematic drawing of the MPF-setup- Adapted from (18).

Two pulsed laser diodes serve as light sources. One is a PicoTA 530 (*PicoQuant* and *Toptica*, Berlin, Germany) which produces laser pulses shorter than 100 ps at full-width-half-maximum (FWHM) and emits at 1060 nm. The frequency is doubled to 530 nm, using a second-harmonic generation module. The maximum power is approximately 2 mW at a repetition rate of 40 MHz. A LDH-D-C-640 (*PicoQuant*) is the second laser, operable in either continuous wave or pulsed mode (< 90 ps at FWHM; maximum output 1.5 mW). The emitted wavelength is 640 nm. The laser pulse is controlled by the

Multichannel Picosecond Diode Laser Driver *"Sepia"* (*PicoQuant*). Thereby, the frequency (10.0 - 80.0 MHz) of the pulses as well as the total laser intensity can be adjusted. In this setup, a laser repetition rate of 26.7 MHz was used. Both Lasers are directly fibre-coupled into polarization-maintaining, single-mode fibres (*Schäfter+Kirchhoff*, Hamburg, Germany). The fibres are connected to a Wavelength Division Multiplexer (*AMS Technologies*, Martinsried, Germany) which acts as beam combiner and joins both laser-beams into one polarization-maintaining single-mode fibre (*AMS Technologies*). The output of the fibre is connected into a fibre collimator (*Schäfter+Kirchhoff*). The beam is directed into the rear part of the microscope by two mirrors with a broadband-coating from 350 to 800 nm (*Thorlabs*, Dachau, Germany). Excitation photons are then reflected into the objective by a dichroic mirror (dichroic 1 in Figure 6, z 532/635; *AHF Analysetechnik AG*, Tübingen, Germany). The beam is focused into the sample by a water-immersion objective (PlanApo VC60x N.A. 1.2; *Nikon*). The sample can be moved with a motorized stage that is either controlled manually with a joystick or automatically from the computer (*Märzhause*r, Wetzlar, Germany). It is possible to mount a nanopositioning stage (*Mad City Labs*, Philadelphia, USA) onto the motorized one in order to take nanoscale scanning images of a sample. The fluorescence light is collected by the same objective and passed through the dichroic mirror 1. A tube lens focuses the light through the side-port of the microscope onto the confocal pinhole (50 µm, *Thorlabs*). Then an achromatic lens (lens 1 in Figure 6, AC254-100-A1; *Thorlabs*) recollimates the focused beam to a beam diameter of approximately 3 mm and guides it to a Polarizing Beam Splitter Cube (*Thorlabs*). This cube splits the light into parallel and perpendicular polarization. The polarized light is then separated into green and red fluorescence by dichroic mirrors 2 (laser beamsplitter 640DCXR*; AHF Analysetechnik AG*). Green photons are reflected while red photons can pass. To eliminate scattered laser light an emission filter is used after the photons are divided by polarization and wavelength. With achromatic lenses (lenses 1 and 2 in Figure 6, AC254-100-A1/-B; *Thorlabs*) the light in each channel is focused onto a Single-Photon-Avalanche-Photodiode (*Perkin Elmer*, Fremont, USA). The individual photons are transformed into TTL-pulses and recorded by four independent and synchronized TCSPC-cards (*Becker & Hickl*, Berlin). Every photon travels the same distance from the microscope to the detector, regardless of its wavelength or polarization. In addition, a camera is attached to the front port for alignment without visual inspection through the oculars. With this setup one is able to distinguish the excitation source, the wavelength, the polarization, the arrival time of every photon and the lifetime of dyes (18).

III.2 Setup Adjustments

III.2.1 Calculation of the Green and Red Confocal Volume

To determine the size of the green confocal volume, several fluorescence correlation spectroscopy (FCS, see chapter III.3) measurements of Rhodamin 6G (R6G) are averaged. The diffusion coefficient of R6G, quantified by 2-focus-FCS, is $D(\mathrm{Rh6G}) = 415 \pm 5$ µm²s⁻¹ (24). To calculate the corresponding volume, the diffusion time τ_D $(0.19 \pm 0.02\ \mathrm{ms})$ and the structure parameter p (7.0 ± 0.5) need to be extracted. The structure parameter p is defined as the ratio of axial length z_0 to lateral length ω_0 of the focus:

$$p = \frac{z_0}{\omega_0}$$

The lateral parameter can be calculated as follows:

$$\omega_0 = \sqrt{4 \cdot D \cdot \tau_D}$$
$$\omega_{0G} = (535 \pm 20\ )nm$$

The effective confocal volume V_G of the green channel is calculated with

$$V = \left(\frac{\pi}{2}\right)^{3/2} \omega_0^2 z_0.$$

If both equations are combined, the following transformation is possible:

$$V = \left(\frac{\pi}{2}\right)^{3/2} \omega_0^3 p$$
$$V_G = (2.12 \pm 0.37) \cdot 10^{-15} L.$$

The confocal volume for the red channel is calculated equivalently by conducting and averaging FCS-measurements with the dye Cy5 ($D = 370$ µm²s⁻¹).

Hence, an averaged structure parameter of $p = 8.1 \pm 0.4$ and an averaged diffusion time of $\tau_D = 0.40 \pm 0.01$ ms results, which leads to following lateral length ω_{0R} and confocal volume V_R of o the red laser:

$$\omega_{0R} = 769 \pm 19\ nm$$
$$V_R = (7.25 \pm 0.36) \cdot 10^{-15} L$$

The overlap of the red and the green probe volumes is given by using a one-fibre, one-pinhole apparatus. The only possibility that the probe volumes do not overlap arises from chromatic aberrations. A way to visualize the point-spread-function and therefore check the overlap of green and red probe volume is to use bead scans like shown in Figure 7 (18).

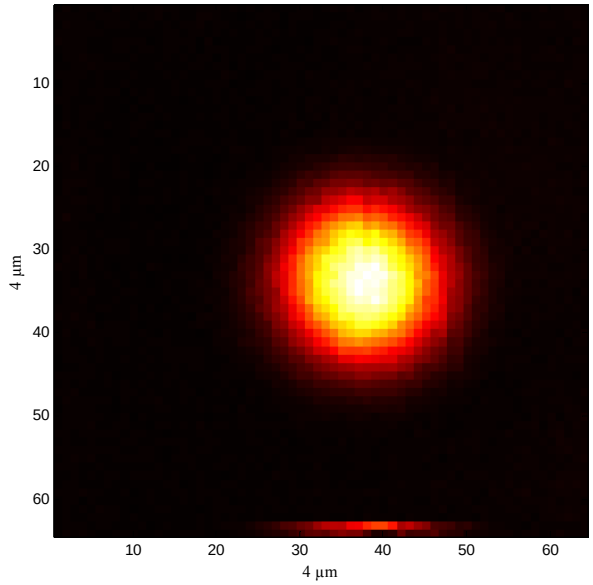

Figure 7 4 µm x 4 µm scan of polymer-fixed microspheres (diameter ~ 200 nm) on the MPF setup.

III.2.2 Determination of the γ-Factor

The correction factor γ mentioned in chapter II.3 is determined by measuring two bilabeled DNAs. One of them shows a high FRET efficiency (b2d1) of approx. 80 %, the other a rather low FRET efficiency (b3d4) of approx. 10 %. The combination of burst analysis and PIE creates a possibility to directly determine the average γ-factor for freely diffusing molecules. The stoichiometry, S provides information over the ratio of the donor and acceptor dyes per molecule. Usually, the inverse stoichiometry is plotted versus FRET efficiency f_E. If the equations for stoichiometry and FRET efficiency are combined, the following expression for γ results:

$$\gamma = \frac{(\Omega - 1)}{(\Omega + \Sigma - 1)}$$

Here Ω and Σ are defined as $\Omega = 1 + \gamma\beta$ and $\Sigma = \beta(\gamma - 1)$. β constitutes the ratio of excitation intensities and absorption cross-sections of donor and acceptor. Ω and Σ can be easily obtained by the means of a linear regression of two different FRET populations (17).

III.3 Fluorescence Correlation Spectroscopy (FCS)

FCS is a method to characterize the dynamics of fluorescent fluctuations. Of primary interest are intensity fluctuations caused by spontaneous deviations of the system from thermal equilibrium, not the emission intensity itself like in other fluorescence experiments. In general, all physical parameters that give rise to fluctuations in the fluorescence signal are accessible to FCS. This enables determination of local concentrations, mobility coefficients or characteristic rate constants of inter- or intramolecular reactions of fluorescently labeled biomolecules in nanomolar concentrations (25).

Classical relaxation methods gain information about the kinetic parameters from the way a reaction system returns back to equilibrium after a perturbation for example with induced temperature or pressure jumps. FCS takes advantage of fluorescence fluctuations, which result from particle movements, conformational changes or chemical or photophysical reactions.

The fluctuations can be quantified in their strength and duration by autocorrelating the recorded intensity signal, a mathematical procedure that gave the technique its name. The **autocorrelation analysis** provides a measure for the self-similarity of a time series signal and therefore describes the persistence of information carried by it. Essential information about processes governing molecular dynamics can thus be derived from the temporal pattern by which fluorescence fluctuations arise and decay. FCS only yields significant results if between non-attached particles spontaneous, non-coordinated fluctuations take place. Though FCS is theoretically independent of concentration, the molecular brightness can affect FCS measurements. By combining the FCS technique with confocal detection, the number of excited molecules is highly reduced due to the mentioned small confocal excitation and detection volumes. Performing an autocorrelation analysis, one effectively compares a measured signal with itself at some later time and looks for recurring patterns.

The correlation analysis can be generalized for two different signals, as common in electronics. In fact, **cross-correlation analysis** (FCCS) generalizes the FCS method. Thus, artefacts introduced by the detector (such as “afterpulsing” of an APD) can be removed by analyzing only the common features of two independently measured signals. There are two applications of FCCS which have proved to be especially effective. First of all, there is the spatial cross-correlation between the fluctuations measured in two separate volume elements.

As a molecule only correlates with itself, this kind of cross-correlation curve will reach its maximum not for small time lags, but rather for the average time a molecule needs to diffuse from one detection volume to the other. Thus, the flow- or transport-velocity of the fluorescent particles can be determined (26). It is also possible to determine velocities of directed sample flows having only one focus by using either cross- or autocorrelation analysis (27). The second application of cross-correlation is the dual-colour mode (28). For this purpose, two spectrally different dyes are excited within the same detection element using two overlapping laser beams and separate detection pathways. Dual-colour cross-correlation is an extremely powerful tool to research interactions between different molecular species.

III.4 Burst Analysis

The Burst Analysis is an approach to determine single pair FRET efficiencies of freely diffusing molecules in solution. Due to Brownian motion the molecules pass the confocal excitation volume. While the molecule passes the focus, a burst of photons is emitted. The number of photons in each bin depends on the time the molecule remains in the confocal excitation volume (up to several milliseconds). As the concentration in single molecule measurements is low (10–50 pM), the probability that two molecules remain in the detection volume at the same time is negligible (< 1 %).

Traditionally, to conduct a burst analysis, only the donor is excited while the fluorescence is detected in both the acceptor and the donor channel. There is just one threshold value, which must be exceeded by the sum of all arriving photons in a certain time interval. Only then a burst is recognized as a molecule (donor criterion).

III.5 Pulsed Interleaved Excitation (PIE)

When conducting two or multicolour experiments, it is often advantageous to know the excitation source in addition to the detection channel. This is possible through pulsed interleaved excitation (PIE). PIE is based on non-continuous excitation of samples containing multiple fluorophores. The dyes are not excited simultaneously but alternating. Consequently, photons which are emitted after a laser pulse excitation are already detected when the following pulse excites another dye in the sample. Figure 8 shows the excitation and detection using PIE schematically in the way it is used during this work.

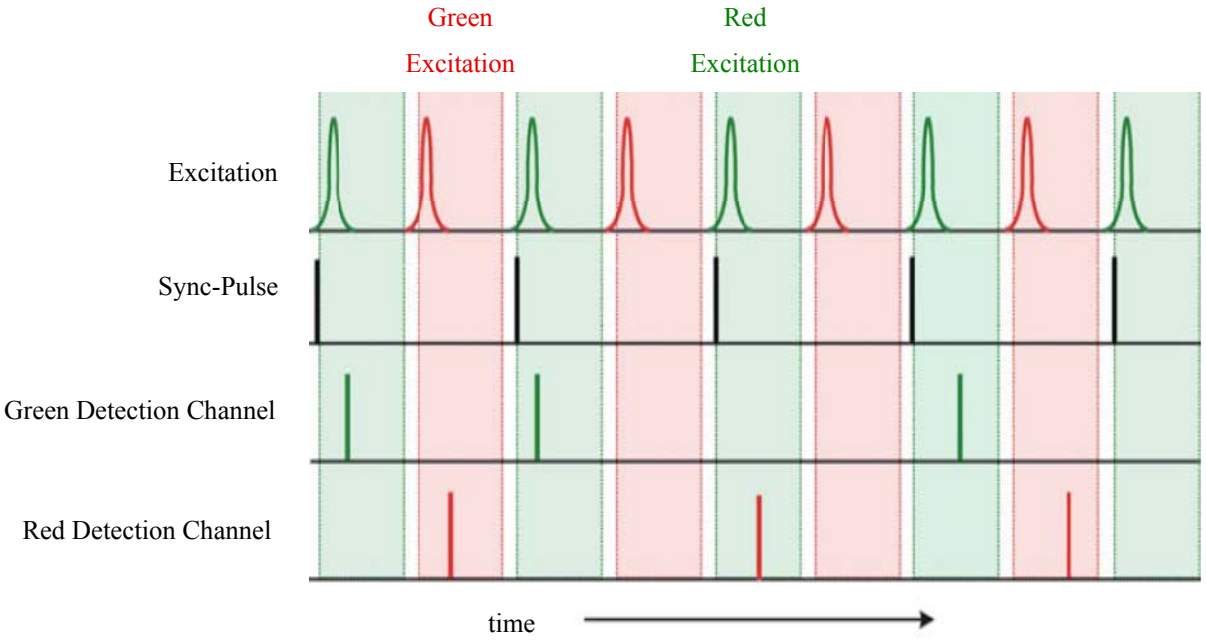

Figure 8 Schematic representation of excitation and detection using PIE. Adapted from (17).

A sync-pulse from the Sepia II (*PicoQuant,* Berlin, Germany) determines the pulse frequency. During a pulse cycle, the sample is alternately excited with wavelengths of 532 nm (green) and 640 nm (red). After excitation, photons are registered either in the green or the red detection channel. Additionally, the time between sync-pulse and detection is recorded.

A histogram from all pulse cycles leads to Figure 9. Both detection channels are displayed in the respective colour. In the illustrated example, the pulse frequency was 27.7 MHz, i.e. the duration of a cycle amounts to 37 ns. The expected time domains (bins) for each excitation are 0–16 ns (red excitation) and 17–32 ns (green excitation). Furthermore, one can find that the pulse frequency cannot be chosen at will, it has to be adjusted to the pulse duration and

the lifetime of the excited state. Otherwise both domains could not be distinguished. The photons within each detection channel can be separated by their excitation source.

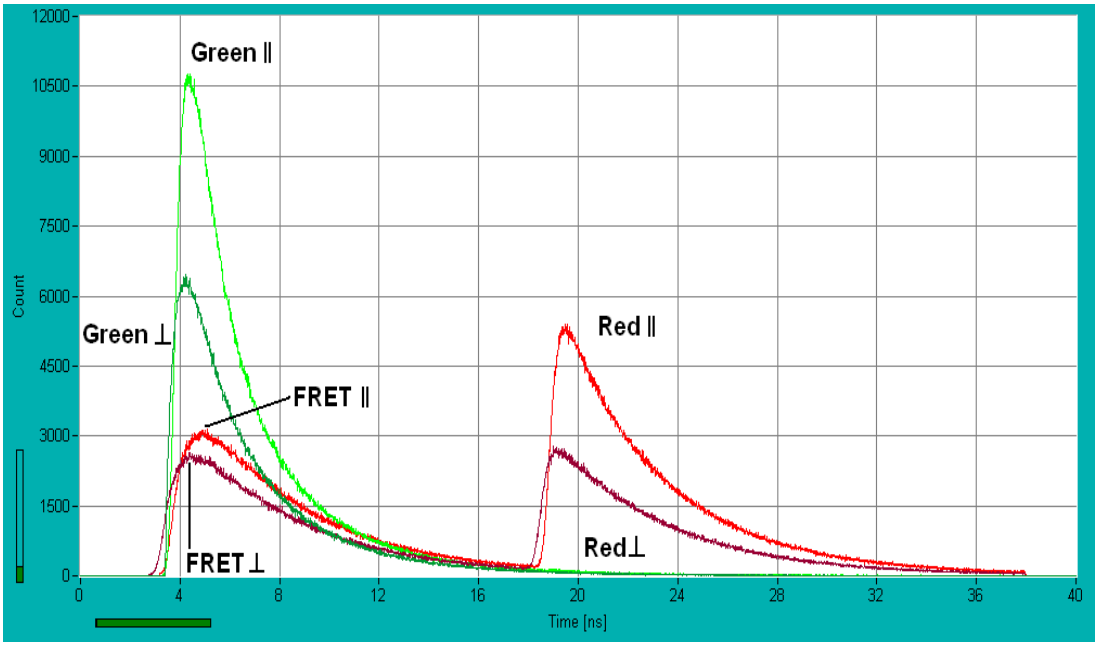

Figure 9 Lifetime histogram of a high FRET DNA sample shown for all four detection channels (red = red detection channel and green = green detection channel; dark colour = ⊥, light colour = ∥). Adapted from (18).

Effectively, there are four possible detection channels for each polarization:

Green detection after green excitation: F_{GG}

Green detection after red excitation: F_{GR}

Red detection after red excitation: F_{RR}

Red detection after green excitation: F_{RG}

Figure 10 displays those four detection channels for one polarization. In the following, the detected photons are assigned to the excitation pulses.

As expected, many photons are registered after excitation and detection in the same channel (F_{GG} and F_{RR}). The intensity of F_{RG} depends on FRET, spectral crosstalk and direct excitation, so the signal strength can vary. Normally, after red excitation no signals are detected in the green detection because neither crosstalk nor direct excitation is possible due to energetic issues.

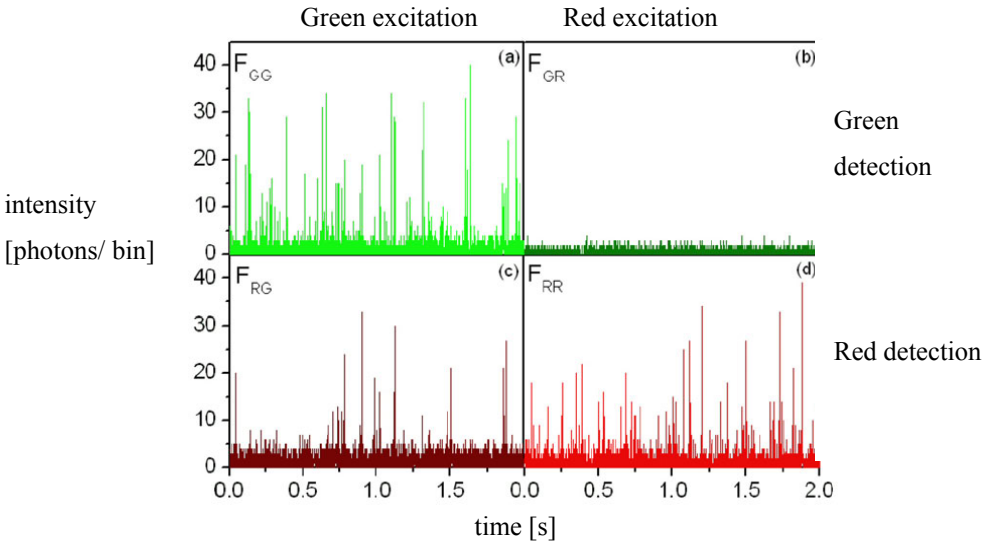

Figure 10 By means of PIE, the detection can be separated into four channels. Adapted from (17)

There are various applications for PIE. For example, differentiation of molecules that are labeled with acceptor and donor fluorophores from molecules that have just one dye attached is possible. If burst analysis (see chapter III.4) is combined with PIE, there is an additional acceptor criterion: The photons in the F_{RR} channel have to exceed a threshold value in a certain time interval, i.e. an active acceptor exists. If this is the case, the donor criterion is controlled to check if a donor exists in the same time interval. Thus, the FRET efficiency is only calculated for molecules which meet both criteria (and hence have an active acceptor and an active donor) (17). Besides, FRET activity between two fluorophores can be excluded by summing up all photons which are detected after green excitation into one combined channel. This turns out to be especially important for cross- and autocorrelation measurements (see chapter VI.3.2). PIE can also be used with three or more excitation sources, where it is possible to determine distances between several fluorophores simultaneously. Thereby, if the three dyes are attached on adequate sites of the observed molecule, information about three different distances can be obtained. This facilitates insight in two- and three dimensional molecular dynamics, depending on the single movements of the molecule. The theory of three-color-FRET is more complex than the one of two-color-FRET, as there are three competitive processes. If dye 1 is excited, an energy transfer to either dye 2 or dye 3 is possible. Furthermore, the excitation energy can be transferred in two steps from dye 1 to dye 2 and eventually from dye 2 to dye 3. Figure 11 displays the possible transfer rates for those processes. Especially challenging is the right choice of dyes for three-color-FRET. On the one hand, the dyes have to be spectrally separated to achieve an unambiguous spectral separation of excitation and emission.

On the other hand, APDs are only sensitive in a certain spectral range. Below 500 nm their sensitivity declines quickly (17). One example for a three-colour-PIE application will be discussed in chapter VI.

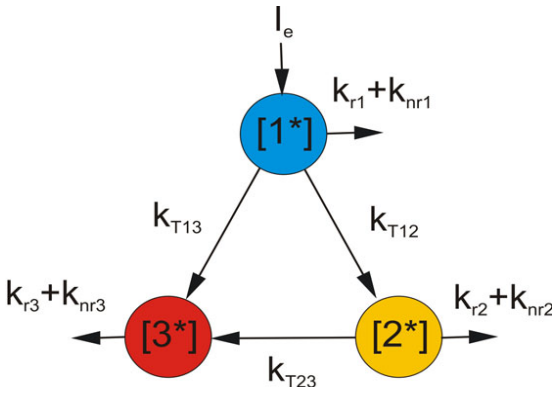

Figure 11 Diagram showing the possible transfer rates between the excited states [1*], [2*] and [3*]. Adapted from (29).

IV Materials and Chemical Methods

IV.1 Stocks and Solutions

IV.1.1 Protein- and DNA Tile-Stocks

Protein Stock	Concentration
DM-MBP 52-298	22 µM
DM-MBP 175-298	224 µM
wt SR-EL	40 µM
V263S SR-EL	40 µM
GroES	240 µM
TBP Cy3/TBP Atto532	400 nM
TBP	5 µM

Table 1 Protein Stocks (kindly provided by the Group of Ulrich Hartl, MPI of Biochemistry, Martinsried and the Group of David Auble, University of Virginia, USA)

The absolute concentration varies from DNA tile stock to DNA tile stock. Each concentration was determined by measuring the absorption at 260 nm on a Nanophotometer (*Implen*, München, Germany).

DNA tile	Base Sequence	bp
1	TACTCGCACCTTCGCTGAGTTTGGACTGTCGGTAGC	36
2	CGTGAGGTGAGTGGGACACCGAAGCCT	27
3	AACCGCTTTGCGTTCCTGCTATCG	24
4	GCTCCGCAGGCTTCGGATTGGCGAAACGCAAGGTGAGGTGAACCGATGCTG	51
5	CGAGGCGTGGTAGCGGGCTATAAAAGGGCGATGGACTCCTGAATCTC	47
6	AGATGCCACCACAGTCACGGATGGACTCACCTCACG	36
7	TACCAGGCTGTAACGGACGATACG	24
8	CGTATCGTTGGTTCTTTTGAACCTGACCTGCGAGTAGAGATTCACCAAACTCAGCGAAGG ACTTGCCAGTACG	73
9	CGTACTGGCAAGTGGTCACCGTTACAGCCTGGTAGTGAGCTTCCTGCTACGG	52
10	CCGTAGCACCATCGCCCTTTTATAGCCCGCTACCTGTCCTGCGAATG	47
11	GCTACCGACAGTGGAGTGGAAGCTCAC	27
12	CGATAGCACCAGATTTTTCTGGACTCCTGGCATCTCATTCGCACCATCCGTGACTGTGGAC TTGGCTACGAC	72

Table 2 Base sequences and length of the 12 used DNA tiles (*IBA GmbH, Göttingen, Germany*).

DNA	Leading Strand Base Sequence	bp
mut	GCCACGTGACCGGGTGTTCCTGAAGTCTAGATGTAAAAGAAGCTTGGGGCGCGTTCGTC CTCACTCTCTT	70
tb1	CTTCACCTTATTTGCATAAGCGATCTATATAAAAGCGCCTTGTACTACCCTGCTCACGCT GTTTTTCCTTTTCGTTGGC	80
tb2	GCCACGTGACCGGGTGTTCCTGAAGGGGGGCTATAAAAGGGGGTGGGGGCGCGTTCGT CCTCACTCTCTTCCGCATCGCTGTCTGCGAGGGCCAGCTGTTGGGGTGAGTA	110

Table 3 Leading strands of labeled control DNAs (*IBA GmbH*); Red and green markings represent the dye position (Red = Atto647N; Green = Atto532); Yellow marking highlights the TBP-binding sites, whereby *mut* exhibits a point mutation A→G.

IV.1.2 Buffers

All Buffer components were dissolved in Millipore water.

Buffer	Components	Concentration/Amount
TAE-Mg Buffer pH 8.0	Tris-acetate EDTA $MgCl_2$	40 mM 1 mM 12 mM
TE Buffer pH 7.5	Tris-HCl EDTA	10 mM 1 mM
LS-Buffer pH 7.5	Tris-HCl KCl $Mg(OAc)_2$	20 mM 20 mM 5mM
BC 100 Buffer pH 8.0	Tris KCl EDTA Glycerin	20 mM 100 mM 1 mM 20 % v/v
Hepes Buffer pH 8.2	Hepes-KOH TCEP	50 mM 20 µM
TBP-working Buffer	$MgCl_2$ Hepes-Buffer BSA PMSF DTT NP40 BC 100 Buffer H_2O	100 mM 25 mM 250 mM 500 µM 2.5 mM 0.25 % v/v 60 % v/v 30.25 % v/v

Table 4 Buffers.

IV.2 Polyacrylamide and Agarose Gel Electrophoresis

Gel electrophoresis is one of the biochemical standard techniques. In this work, both agarose and polyacrylamide gel electrophoresis (PAGE) were used. Agarose gel electrophoresis is used to separate the DNA construct of interest from smaller DNA tiles in order to conduct a gel extraction (IV.3) afterwards. Therefore, a 2% agarose solution (agarose diluted in TAE-Mg Buffer) is brought to the boil and afterwards poured into the adequate chamber.

Non-denaturating polyacrylamide gels (Native-PAGE) serve the purpose to control the composition of a given DNA- or protein solution without denaturating the compounds. The DNA fragments or proteins are separated by weight. In order to get two 6% acrylamide gels the following compounds are mixed and poured in two 60 mL gel chambers:

Acrylamide	18 mL
TAE-Mg Buffer	100 mL
APS (radical initiator)	1.2 mL
TEMED (cross linking agent)	0.12 mL

For both PAGE and Agarose gel electrophoresis, a visible negatively charged loading buffer is added to the samples. The probes are then resolved by electrophoresis for 2 h at 200-300 V and 4 °C.

The gels were stained for 30 min in SYBR-Gold and visualized on an UV-Gel-Imager (*Bio-Rad,* München, Germany).

IV.3 DNA-Gel-Extraction

Gel extraction is a method to separate the DNA fragment of interest from either larger or smaller side products. In this case, the synthesized DNA fragment consists of 512 base pairs and needs to be separated from fractions with less molecular weight (i.e. in our case incomplete DNA structures).

A 3%-agarose gel is loaded with the DNA-solution of interest. After running a common gel electrophoresis, the high molecular band is cut out and put into a spin column tube (*Bio-Rad*). After 5 min at -40 °C the gel piece is centrifuged 30 min at 13.000 rpm. During the centrifugation the liquid compounds (i.e. the solvent and the solved DNA) pass the filter due to the centrifugal forces. The solid components (i.e. the polymerized agarose) stay in the filter. This gel extraction technique is also known as the “freeze and squeeze method”.

IV.4 Ethanol Precipitation

In case the concentration of a DNA fragment turns out to be too low for further experiments it is a convenient technique to precipitate the DNA with ethanol. Therefore sodium acetate is added to the given DNA-solution to a final concentration of 0.3 M. The following addition of ice-cold ethanol (at least the double volume of the DNA solution) displaces the H_2O molecules and thus the screening of charges by water is disrupted. Hence, electrical attraction between the phosphate groups of the DNA backbone and the added sodium ions becomes strong enough to form stable ionic bonds and the DNA precipitates from the solution. During an incubation time of approximately 15 min at 0 °C most of the DNA should crystallize.

In the next step, the solution is centrifuged (14.000 rpm, 30 min) to collect the crystallized DNA at the bottom of the tube. After centrifugation the supernatant solution is removed leaving a pellet of crude DNA. If the pellet is air-dried, the DNA is suspended in the desired amount of TAE-Mg Buffer. The amount of Buffer depends on the pellet size, 20 µL are common in our case.

V Exploring the GroEL/ES Chaperonin System

Molecular chaperones are protein complexes which assist the non-covalent folding and unfolding of macromolecular structures like other proteins. There are many different families of chaperones; each family acts to aid protein folding in a different way. In general, chaperones are believed to facilitate or promote the folding of proteins which are unable to fold on their own under cellular conditions. In bacteria like *Escherichia coli*, many of these proteins are highly expressed under conditions of high stress, e.g. when placed in high temperatures. For this reason, the term "heat shock protein" (HSP) has historically been used to name these chaperones. The most exhaustively studied chaperone is GroEL. GroEL is a member of the HSP60 family of promiscuous type-I chaperonins found in prokaryotes and in eukaryotic mitochondria. Chaperonins are a class of hollow cylindrical chaperones which assist the folding of a subset of newly-synthesized proteins in an ATP-dependent manner. These hollow cylinders can completely enclose the majority of their protein substrates. While held within this container, proteins continue folding in some circumstances, at what appears to be an accelerated rate. Together with heat shock proteins like GroES (HSP10), DnaK (HSP70) and DnaJ (HSP40) and the nucleotide exchange factor GrpE, GroEL performs regular cell maintenance and is present at high concentrations even in the absence of external stress (30, 31). Figure 12 displays the mechanism of the GroEL/GroES system.

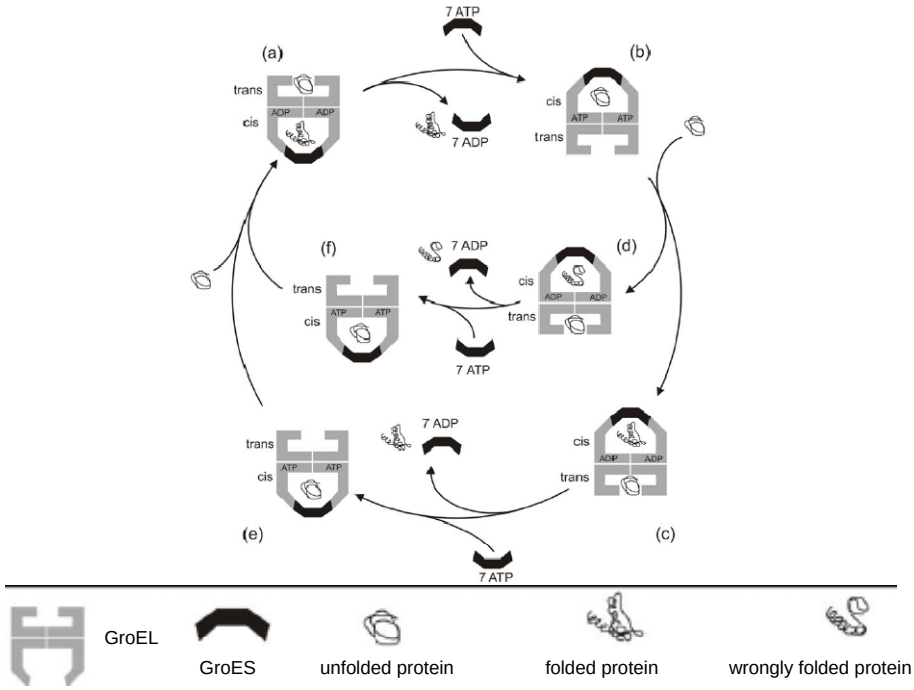

Figure 12 Mechanism of *Escherichia coli* GroEL/GroES system A vertical section of the GroEL double-ring is shown representing the three-domain structure of the GroEL subunits. Adapted from (17, 32).

A large volume of experimental and theoretical work has been undertaken to understand how chaperones like GroEL can assist protein folding in the cell. The most accepted explanation seems to be the simplest: GroEL, like most other chaperones, helps proteins fold by preventing aggregation. However, there is evidence that under some conditions this chaperonin system can also play a more active role in protein folding (33).

GroEL is a 800 kDa cylindrical complex with ATPase activity consisting of two heptameric rings of 57 kDa subunits, each ring forming a central cavity to bind nonnative proteins. The subunits are divided into three domains (34-36). The apical domain forms the ring opening and engages in multiple contacts with substrate protein via hydrophobic amino acid residues exposed toward the central cavity. Figure 13 shows the amino acid residues involved in protein binding to the apical surface of a GroEL ring subunit. The apical domain is connected by a hinge-like intermediate domain to the equatorial ATPase domain. The co-chaperone, GroES, is a dome-shaped heptameric ring of 10 kDa subunits, which contact the apical GroEL domains via flexible loop sequences (37). Thereby, GroES caps the opening of the GroEL cylinder (38).

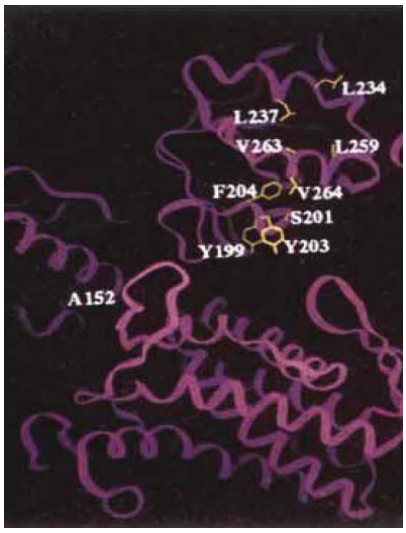

Figure 13 Location of amino acid residues on the apical surface of a 57 kDa GroEL subunit involved in polypeptide binding. Adapted from (34).

About 85 proteins were found to be strictly dependent on GroEL for folding in *Escherichia coli*. While it has long been known that the GroEL cage can prevent the aggregation of substrate proteins during folding, it is now clear that the chaperonin actually accelerates the folding of certain substrate proteins. A detailed study of the mechanism of folding would include the observation of occurring kinetics. Therefore the discrete steps of the whole folding mechanism must be characterized, e.g. the initial bound state of the

substrate to the chaperonin complex, specific kinetically trapped intermediate states accumulated during the folding process and conversion between the unfolded, intermediate and folded states (39). The following subchapters will lead to a method for characterizing the initial bound state of a GroEL/ES substrate protein and present a device to observe the chaperonin system in non-equilibrium.

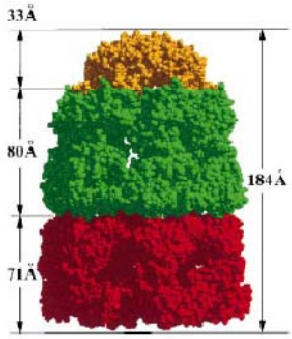

Figure 14 Van-der-Waals space-filling model of the entire GroEL/ES complex in a side view; Red: *trans* GroEL ring; Green: *cis* GroEL ring; Gold: GroES Adapted from (38).

V.1 MBP as a Substrate of the GroEL/GroES-System

The maltose-binding protein, MBP (Figure 15) is a 41-kDa protein that binds maltose tightly in its native state. MBP has several properties that make it desirable as a folding substrate for GroEL. It is monomeric and the *in vitro* folding reaction of MBP has been extensively characterized (40). In addition, formation of the native state results in a dramatic enhancement in intrinsic tryptophan fluorescence, making it possible to continuously monitor the formation of native protein as both GroEL and GroES are devoid of tryptophans.

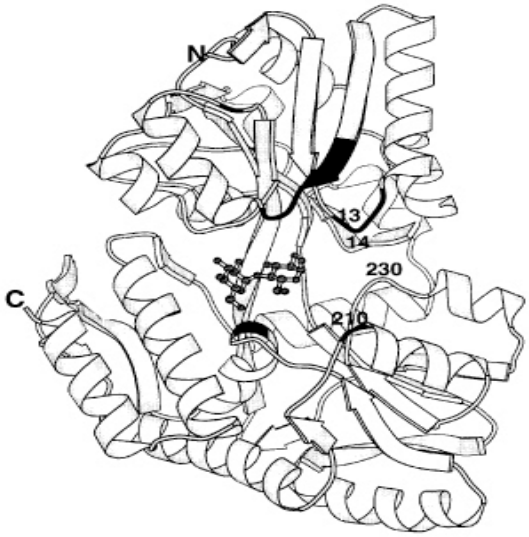

Figure 15 Ribbon-style drawing of MBP. Taken from (40).

Wild-type MBP is not a suitable GroEL model-substrate as it folds efficiently in the absence of chaperones. It was shown that the rate of folding of a dual-point mutant of MBP, which renatures slowly in the absence of GroEL, is significantly enhanced by the addition of GroEL, GroES and ATP. Further destabilization of the native MBP conformation yields substrates whose folding is strictly dependent on GroEL and GroES (41, 42).

DM-MBP is a double mutant of the maltose-binding protein containing mutations V8G (valine replaced by glycine) and Y283D (tyrosine replaced by aspartic acid) in the N-terminal domain. Spontaneous folding of this protein is slow ($t_{1/2}$ of ~ 20 min) but GroEL/GroES accelerates this process by approximately a factor of ten (40). Not every substrate protein is processed equally by GroEL, hence there are different populations, varying in their folding status. To obtain insight into the conformational states populated during chaperonin-assisted folding, Sharma *et al*. (32) labeled single-pair cysteine mutants of DM-MBP with Atto532 as the donor and Atto647N (*AttoTec*, Siegen, Germany) as the

acceptor dye for single-molecule and ensemble FRET experiments. Measurements were carried out with three double-cysteine mutants which differ in the spatial position between both dyes. During this thesis, two of these dye-mutants were used: DM-MBP 52-298, which is a double-cysteine mutant at amino acid position A52 (alanine) and P298 (proline) and DM-MBP 175-298 with cysteine mutation K175 (lysine) instead of A52. In the protein's native state, the distance between the mutated residues is 33 Å for combination 52-298 and 32 Å for 175-298. The dyes are attached to these cysteine residues, so that ideally each protein bears a donor and an acceptor fluorophore. Figure 16 shows an overview of several potential dye positions, containing as well A52, K175 and P298.

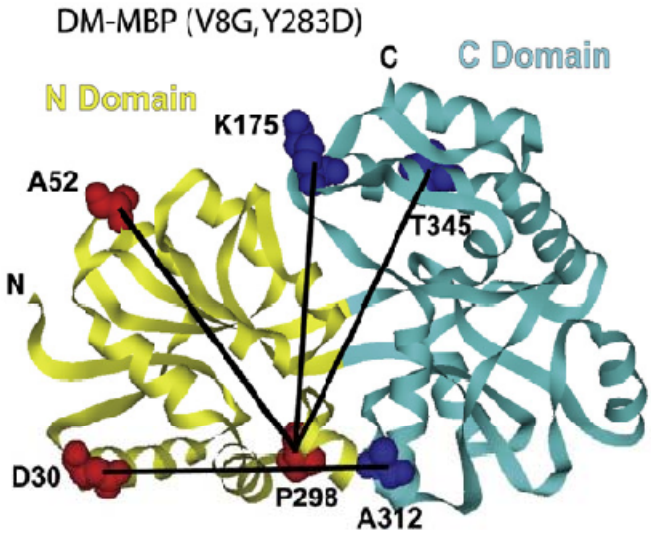

Figure 16 Possible dye positions on DM-MBP. Adapted from (32).

V.2 Initial Binding of DM-MBP to GroEL and its Mutants

Substrate proteins like DM-MBP bind on the apical surface of GroEL. After the binding of ATP and the co-chaperone GroES, the proteins get encapsulated inside the GroEL cavity where they start folding. Initial binding of the substrate causes its partial unfolding, putatively caused by the multivalent binding to different apical domains of the GroEL molecule.

Nonnative substrate binding to one or more of the seven GroEL apical domains has been studied by Farr *et al.* (43). Aim of Farr's work was to show, how many of the seven possible binding domains on GroEL a substrate protein actually needs. Therefore, his research group produced eleven GroEL mutants. The mutants were based on a concatamer of GroEL – i.e. GroEL is produced as one single molecule – which enable to express binding-deficient and -efficient subunits arranged in a particular pattern. Figure 17 displays Farr's binding site mutants.

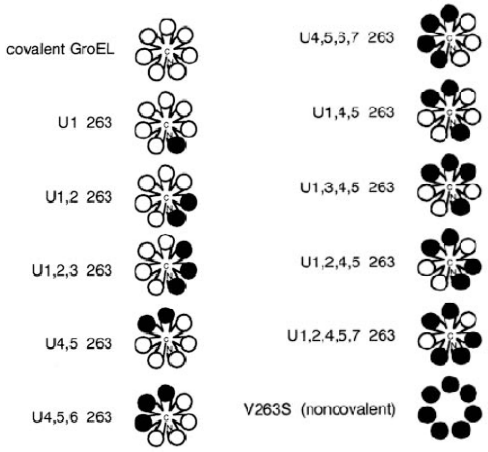

Figure 17 GroEL binding site mutants. The black colored circles represent the domains bearing a mutated binding site. Adapted from (43).

Farr and his colleagues conducted binding experiments with two different proteins, malate dehydrogenase (MDH) and Rubisco. For both proteins, a nearly full extent of binding was observed with a complex with only three consecutive wild-type subunits. Figure 18 shows the binding rate of the substrate proteins to the various GroEL mutants.

But despite Farr's results, it is not clear whether the initial unfolding of substrate proteins plays an active role in the fast refolding kinetics mediated by GroEL. Actually, unfolding could be important to get proteins out of so-called folding traps. Based on the FRET-measurements with bilabeled DM-MBP of Sharma *et al.* (32), the binding of DM-MBP 52-298 and 175-298 to GroEL mutants addresses this question.

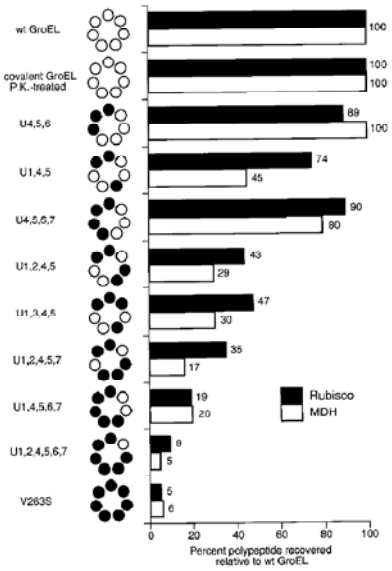

Figure 18 Binding of nonnative Rubisco and MDH to mutant GroEL. Adapted from (43).

On wild-type GroEL, DM-MBP is stretched when it binds, resulting in a larger distance between the donor and the acceptor dye and hence in a lower FRET efficiency. The question is how DM-MBP behaves on mutant GroEL. However, the mutants are expected to stretch proteins to various extents.

For this thesis, single-ring GroEL (SR-EL) was used. The GroEL/GroES system normally "cycles" due to its two back-to-back linked subunits, which both can theoretically bind a substrate (44). Actually, the substrate just binds to one side, gets capsulated by ATP and GroES binding, folds in the cavity and is then released by a conformational change (32). This alternation of conformations would not be possible if it was not for the identical subunit on the backside. As SR-EL consists only of one subunit, the substrate stays significantly longer in the cavity, allowing snapshots of the encapsulated protein to be easily collected.

In this thesis' experiments the binding of two differently labeled DM-MBP mutants to the V263S all over mutant concatamer single-ring GroEL (V263S SR-EL) was observed. To have a bench mark for the V263S SR-EL results, it is necessary to carry out measurements with wild-type concatamer single-ring GroEL (wt SR-EL) as well. The labeled substrate proteins are primarily diluted in denaturant-containing buffer (3–6 M guanidinium chloride). In a last step they are brought to a final concentration of approx. 60 pM in a 6 μM SR-EL solution.

Figure 19 shows the histograms of DM-MBP 52-298 on the left and DM-MBP 175-298 on the right bound to wt SR-EL. The FRET efficiency distributions of DM-MBP 52-298 and DM-MBP 175-298 bound to SR-EL differ slightly from those of Sharma *et al.*

Indeed, as well in Sharma's publication as in the according histograms below a minor low FRET population and a major high FRET population are visible. But the low FRET populations obtained here are unambiguously lower. Both DM-MBP mutants apparently do not bind properly to SR-EL or are binding without being stretched.

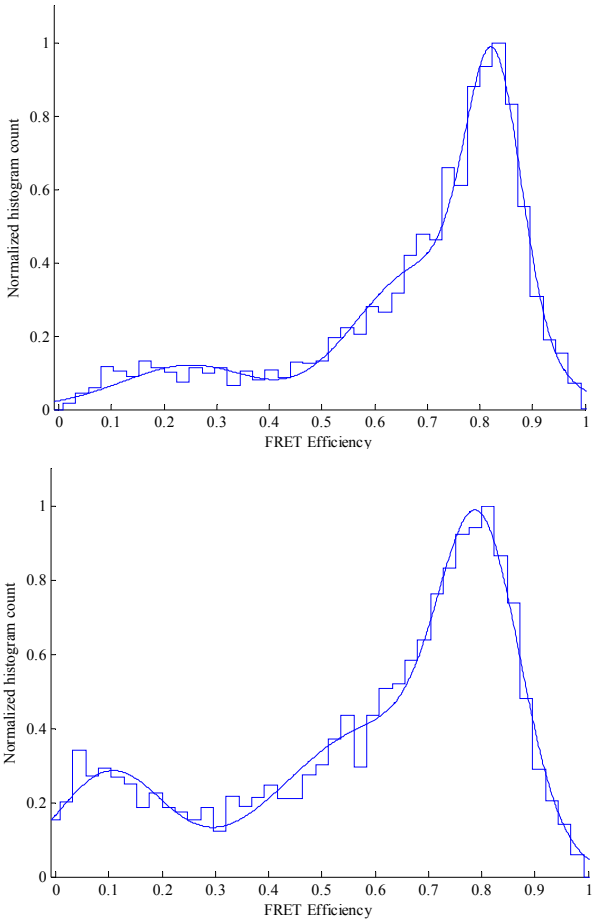

Figure 19 Single-molecule FRET efficiency distribution DM-MBP bound to wt SR-EL; Left: DM-MBP 52-298; Right: DM-MBP 175-298. The histograms were fitted empirically by a three Gaussian fit.

How MBP 52-298 and DM-MBP 175-298 act in presence of mutant V263S SR-EL is shown in Figure 20. The mutations in the binding sites do not affect the FRET efficiency distribution of the DM-MBP 175-298 construct in a stringent way, though the low FRET subpopulation visible in Figure 19 (wt SR-EL) decreased a bit. In contrast, DM-MBP 52-298 binding to V263S SR-EL shows a significant shift in the FRET efficiency distribution. A major low FRET population compared to a major high FRET population when the protein interacts with wt SR-EL. Evidently, the two fluorophores of DM-MBP 52-298 more distant from each other, due to a conformational change of the native protein structure.

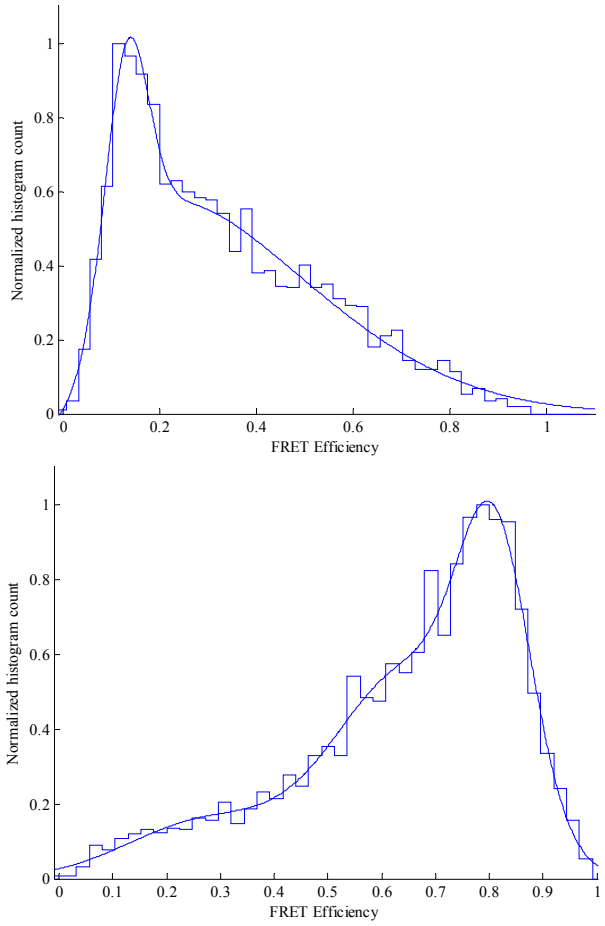

Figure 20 Single-molecule FRET efficiency distribution DM-MBP bound to V263S SR-EL; Left: DM-MBP 52-298; Right: DM-MBP 175-298. The histograms were fitted empirically by a two and a three Gaussian fit, respectively.

As a control measurement, binding of DM-MBP 52-298 to double ring GroEL was investigated as well. The spFRET measurement led to the following histogram (which complies with the results of Sharma *et al.*).

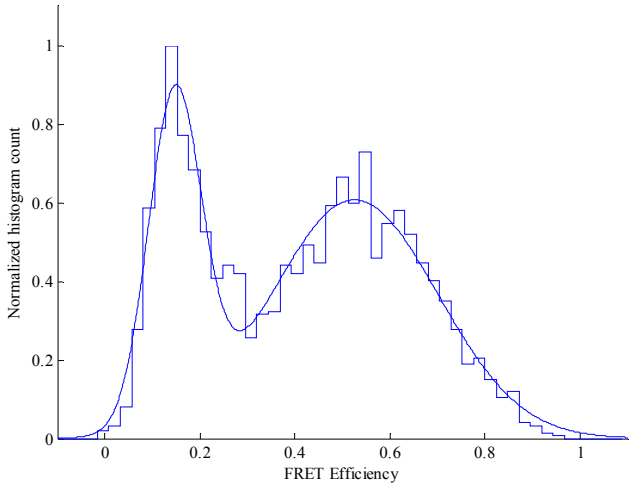

Figure 21 Single-molecule FRET efficiency distribution DM-MBP 52-298 bound to wt GroEL. The histogram was fitted empirically by a two Gaussian fit.

To investigate whether the proteins are bound to the single rings, the diffusion time of the complexes was determined by autocorrelation of the FRET channels (GR1+GR2xGR1+GR2; chapter VI.3). Followings figures display the according ACFs for each protein-SR-EL combination.

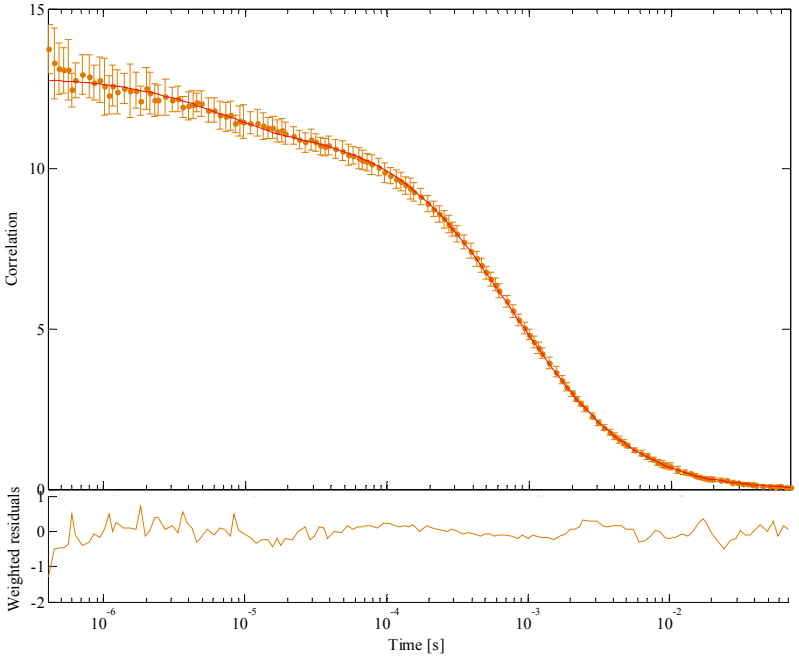

Figure 22 ACF (FRET channels) of DM-MBP 52-298 bound to wt SR-EL.

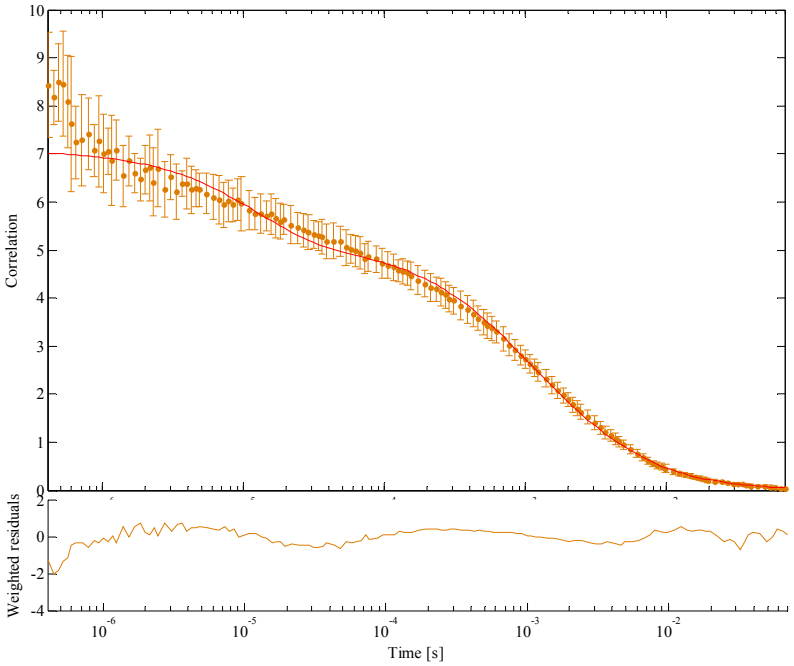

Figure 23 ACF (FRET channels) of DM-MBP 52-298 bound to V263S SR-EL.

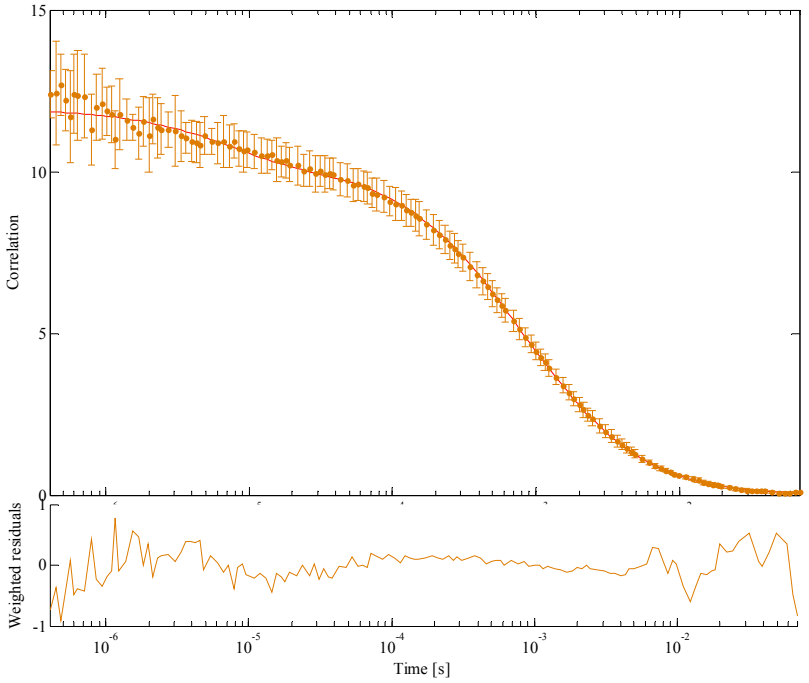

Figure 24 ACF (FRET channels) of DM-MBP 175-298 bound to wt SR-EL.

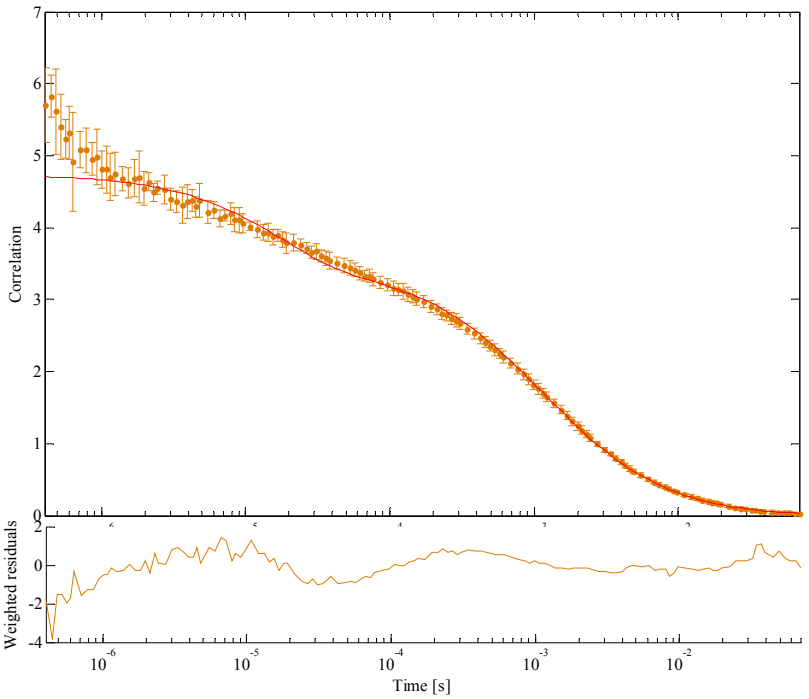

Figure 25 ACF (FRET channels) of DM-MBP 175-298 bound to wt SR-EL.

Thus, following diffusion times τ_D result:

$\tau_D(52/\text{wt}) = 0.78 \pm 1.2 \cdot 10^{-2}\text{ms}$ $\tau_D(52/\text{mut}) = 1.18 \pm 7.3 \cdot 10^{-2}\text{ms}$

$\tau_D(175\ /\text{wt}) = 0.81 \pm 2.2 \cdot 10^{-2}\text{ms}$ $\tau_D(175\ /\text{mut}) = 1.17 \pm 6.0 \cdot 10^{-2}\text{ms}$

An ACF of DM-MBP 52-298 (Figure 26) provides a reference point for the diffusion time.

$$\tau_D(52) = 0.85 \pm 3.6 \cdot 10^{-2}\text{ms}$$

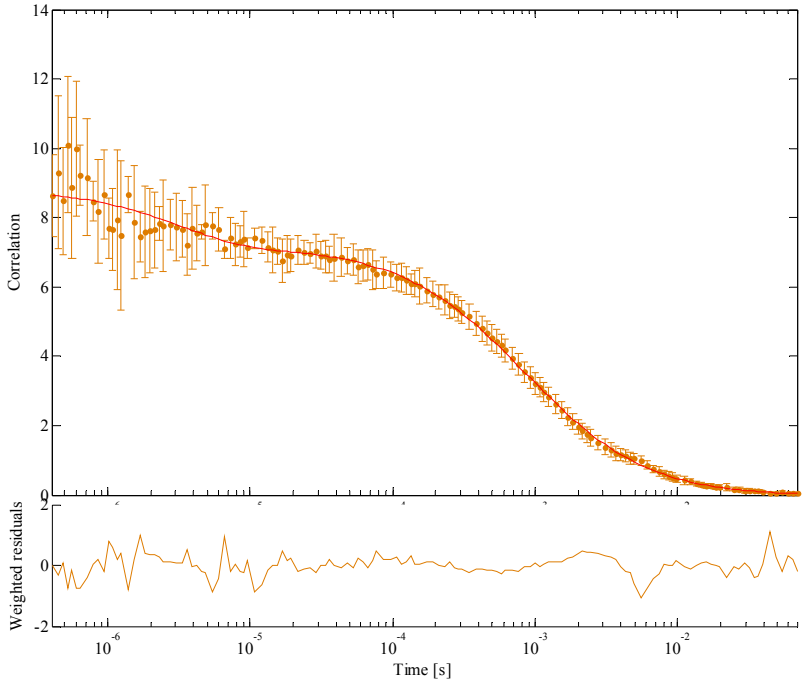

Figure 26 ACF (FRET channels) of DM-MBP 52-298.

Deviations in diffusion time (like $\tau_D(52) > \tau_D(52/\text{wt})$) can be traced back to minimal deviations in the focus position. The DM-MBP 52-298 sample was not measured on the same day as the SR-EL samples. Nevertheless the resulting diffusion time of DM-MBP 52-298 constitutes a sufficient reference point for the SR-EL measurements.

V.3 Discussion

It is known that both seven-subunit rings of GroEL are essential to complete the GroEL/ES reaction cycle (45). The measurements with wt SR-EL compared to the control measurement with wt GroEL disclose that already the initial binding is affected by the missing subunit ring. When DM-MBP 52-298 binds to GroEL, the protein gets stretched due to the binding sites on the apical surface of the chaperonin subunit. Thus, the distance between the two dyes – attached at positions A52 and P298 – exceed the Förster radius and a major low FRET population is observed.

In contrast, a major high FRET population is observed in the corresponding SR-EL measurements. There are two main explanations for this observation: either DM-MBP binds to SR-EL in a folded conformation or it does not bind at all. The high FRET population visible in the DM-MBP 175-298 histogram emphasizes these assumptions. FCS measurements result in almost the same diffusion time (~ 0.8 ms) for both freely diffusing DM-MBP 52-298 and DM-MBP 175-298 in a SR-EL solution, so clearly DM-MBP does not interact with SR-EL. GroEL-bound DM-MBP e.g. features more than twice the diffusion time as non-bound MBP. These results lead to the conclusion that the used stock of wt SR-EL was contaminated.

Interestingly, the V263S SR-EL measurements of DM-MBP 52-298 and DM-MBP 175-298 entail two completely different FRET efficiency distributions: A major low FRET population for DM-MBP 52-298 and a major high FRET population for DM-MBP 175-298. Both, DM-MBP 52-298 and DM-MBP 175-298 have a longer diffusion time when bound to V263S SR-EL (~ 1.2 ms). These diffusion time values enforce the assumption that binding affinity to the mutant is higher.

The low FRET population for DM-MBP 52-298 is unexpected as the mutant SR-EL has a point mutation in each of the seven subunits' binding site that is expected to eliminate interactions between GroEL and its substrates. It is possible though, that by abolishing a strong interaction (V263 on GroEL) a hidden interaction is revealed which eventually results in stretching of the distance vector 52-298 on DM-MBP. On the grounds of the fact, that the distance of the labels on DM-MBP 175-298 do not exceed the Förster distance a possible new revealed interaction affects the MBP amino acid residues around position A52.

V.4 Construction of a Coaxial Mixer

As already mentioned at the beginning of this chapter, a detailed study of the mechanism of folding would include the observation of kinetics. Until now, mostly equilibrium measurements of the GroEL/ES system have been conducted. Thereby, no or just marginal information about intermediate states is obtained. Non-equilibrium measurements can fill this gap of information. Mixer systems with single molecule sensitivity facilitate observation of systems in non-equilibrium, provided the compounds are mixed quickly. This is difficult in microfluidic systems because of the laminar flow conditions in this regime. A continuous-flow mixing device developed by Hamadani and Weiss enables monitoring of conformational changes of biomolecules at the single-molecule level within a response time of circa 10 ms. The sample fluids can be hydrodynamically focused in three dimensions which creates areas where diffusional mixing is rapid and efficient (46). In order to determine both the distance-to-time transfer and the instrument response function of the device, Hamadani and Weiss characterized its fluid flow and mixing properties using FCCS velocimetry and finite element fluid dynamic simulations. They applied the coaxial mixer to single molecule FRET protein folding studies of Chymotrypsin Inhibitor protein 2 (CI2). The resolution of the denaturant-dependent nonspecific collapse of the unfolded state was achieved both on spatial and temporal levels. Therefore a sample of a bilabeled (Alexa488 and Alexa647) unfolded CI2-construct in a denaturant-containing buffer was placed in the inner capillary. Flow through the latter was manually produced using a pressurized syringe, while a flow of renaturating buffer through the square outer capillary was gravity-driven via a height differential between the diluent and exit reservoirs (Figure 27). The diluent and exit reservoir fluid heights were manually updated to maintain stable flow and velocity profiles.

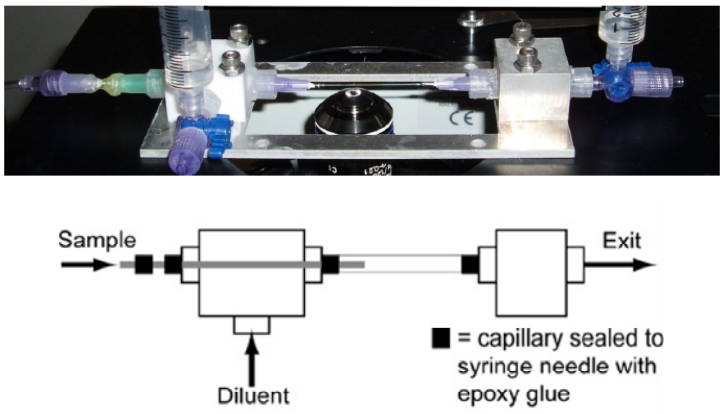

Figure 27 Mixer setup and schematic top view of the coaxial mixer, showing the different reservoirs. Adapted from (46).

As already mentioned, the sample stream is hydrodynamically focused by the exterior one. Due to the high difference of denaturant concentration in outer and inner flow, the denaturant diffuses away from the sample stream. This release of denaturant allows the nonspecific collapsing of CI2, which is detected as a change in the FRET signal (19). Figure 28 illustrates the hydrodynamic focusing of the sample stream.

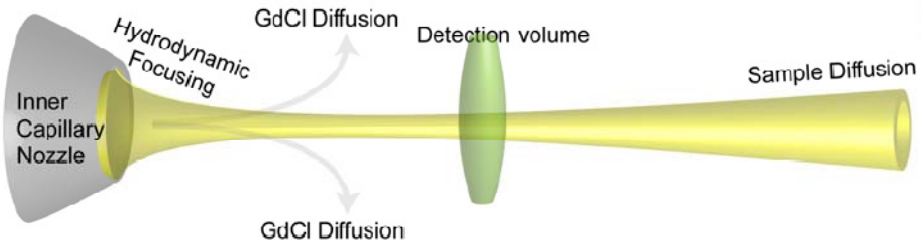

Figure 28 A close-up of the mixing region illustrating hydrodynamic focusing of the sample stream. Adapted from (46).

All mixers are constructed using custom-made aluminium baseplates (Workshop of Chemistry Department, LMU, München) ,Teflon or aluminium T-junction connector blocks, poly-propylene 1/8-NTP male LEUR-LOCK connectors, 10 mL syringes for diluent and exit reservoirs, 300 µm inner diameter (ID)/600 µm outer diameter (OD) square outer capillaries (*Vitrocom*, Mountain Lakes, NJ, USA), and 250 µm OD round inner capillaries (*Vitrocom*) pulled to have defined nozzles with 5–10 µm inner diameters using a self-constructed filament pipette puller (kindly provided by J. Michaelis). The diameters vary with the slope of the heating ramp. Assembly of the mixers is conducted under a conventional light microscope using epoxy minute adhesive (*Weicon*, Münster, Germany) to seal both the inner and outer capillaries to opposite sides of the T-junction connector block. One needle (21G; *B.Braun*, Bethlehem, PA, USA) is carefully glued to the inner capillary, two needles (16G; *BD*, Franklin Lakes, NJ, USA) to the outer capillary to create a macroscopic port for sample solution injection and to protect it from mechanical strain and breaking. In order to optimize the measurement conditions, the square outer capillary has to be positioned perpendicularly to the laser beam and the inner capillary had to be centred within the outer capillary. These steps were carried out under a light microscope, just to verify the flow through both capillaries was running smoothly. Before all experiments, each mixer was thoroughly rinsed with acetone, methanol and water to remove all contaminating fluorescent species and to purify the nozzle from occluding particles.

During a rinse step, pressure needs to be imposed alternately upon two syringes (coupled to the LEUR-LOCK connectors), one at each end of the outer capillary. In addition, all buffers and samples have to be filtered before being used to minimize clogging during the measurements. The mixer can be mounted on a piezo scanning stage (*Mad City Labs*) via several clamps.

In order to calibrate the mixer, several measurements with high FRET DNA labeled with Atto488 and Atto635 were conducted at a two-color PIE setup (488 and 565 nm lasers). DNA was loaded into the sample reservoir (see Figure 27) at a concentration of 60 pM and a volume of 200 µL. The foci of the laser beams were placed directly in front of the nozzle for a 30 min measurement. Primarily, the sample flow is driven manually. When the first photons are detected, constant flow is provided by the hydraulic thrust of a water-filled syringe which is connected to the sample reservoir via an air-filled plastic hose. The resulting histogram of the DNA's FRET distribution is displayed in Figure 29. Measurements ran with a constant DNA concentration in the sample flow. This can be examined during a measurement via a high resolution countrate display (written in *LabVIEW* by V. Kudryavtsev). Via a nanoscale scanning stage the laser foci were positioned 10 µm away from the nozzle in order to control the sample concentration. At this position no photons could be detected. From this it is possible to infer that further mixer experiments have to be conducted with different initial concentrations of the sample. A higher initial concentration e.g. – in order to detect photons at position 10 µm – leads to non-single-molecule concentration at position 0 µm (directly in front of the nozzle).

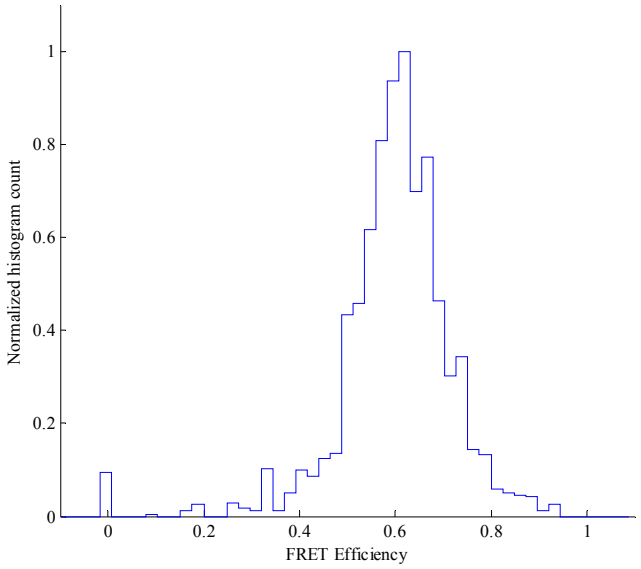

Figure 29 Single-molecule FRET efficiency distribution of a high FRET DNA labeled with Atto488 and Atto 635.

VI Monitoring Protein-DNA Interaction

Interactions between proteins and DNA play an important role in many somatic processes. Among them DNA packaging (involved proteins: histones), DNA replication (e.g. helicase and DNA polymerase), several signal transduction pathways (e.g. nuclear hormone receptors) and DNA transcription. One of the DNA-protein interactions during transcription was investigated in these studies. The TATA box-binding protein (TBP) initiates transcription by binding to a certain sequence on the DNA and thus recruiting more proteins to bind. Most of the DNA-protein interactions are DNA sequence specific and consist of several proteins which eventually form a DNA-binding complex. The involved proteins and their order of binding are usually well characterized. Compared to this research level, the investigation of the binding dynamics seems not very sophisticated. For TBP-DNA interaction e.g., there are models for the binding dynamics, but yet none of them could be verified *in vitro*. Hence, a device to monitor DNA-protein interaction by spFRET measurements was designed and synthesized during these studies.

VI.1 The TATA Box and Its Binding Protein

An enzyme named RNA polymerase reads discrete DNA sections (genes) and synthesizes the appropriate RNA strand concurrently. To transcribe genes the RNA polymerase must detect the correct starting postion on the genetic material. DNA templates contain regions called promoter sites. These sites bind RNA polymerase and determine where transcription begins. Promoter sites on eukaryotic genes have a TATAAA consensus sequence, called TATA box or Hogness box. RNA polymerase does not just bind to the TATAAA-sequence directly. Initially, it is necessary that the so-called Active Transcription Complex assembles around the TATA box. The key initial event is the recognition of the TATA box by the TATA box-binding protein (TBP), a 30 kDa component of a 70 kDa transcriptional factor complex.

TBP is a saddle-shaped protein consisting of two similar domains (see Figure 30). The DNA binds to the concave surface of TBP. This binding induces large conformational changes in the bound DNA: the double helix is unwound to widen its minor groove. This widening enables an extensive contact between the DNA's minor groove and the ß strands of TBP (colored green in Figure 30 B). Hydrophobic interactions are prominent at this interface. Among other interaction, four phenylalanine residues are intercalated between base pairs of

the TATA box. As AT-rich sequences of dsDNA are quite flexible, TBP binding results in bending of the DNA (47, 48).

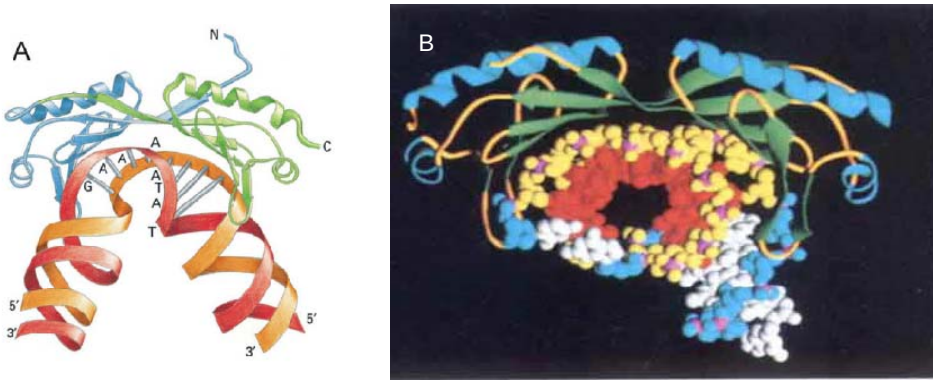

Figure 30 Three-Dimensional Structures of TBP bound to DNA: (A) Adapted crystal structure, which shows how TBP binds to the minor groove of the DNA (47); (B) Original Crystal structure of TBP-DNA-binding. Adapted from (49).

According to literature (47), TBP binds 10^5 times as tightly to the TATA box as to noncognate sequences. The dissociation constant of the complex is approximately 1 nM. Recently van Werven *et al.* (50) discovered, that the TBP turnover is regulated by protein factors rather than DNA sequences. Furthermore they argue that TBP turnover is an important determinant in regulating gene expression.

There are many techniques used to observe DNA-TBP-interactions. Some restrict themselves to the DNA bending, and thus to the TATA box flexibility (51). Other methods observe the dynamics after TBP-binding (52, 53). An interesting starting point is the conformational change of DNA due to TBP-binding. There are many crystal structures of the TBP-DNA-interaction, but these are merely snapshots. If existing, DNA dynamics cannot be resolved in this way. Single-molecule measurements constitute a promising approach, as they enable an observation of the conformational changes of single DNA-TBP-complexes. The aim of this thesis was to synthesize a DNA construct which can deliver three-dimensional conformational information using a three-color-PIE setup (see also chapter III.5).

VI.2 DNA-Constructs Beyond the Double-Helix

Nature shows how amazingly stable forms DNA can adapt. For instance, there is an average of 25 hydrogen bonds within each complete turn of the DNA double helix providing a stability of binding about as strong as what a covalent bond would provide. Nowadays, DNA is a well-established nanoscale building block that self assembles due to specific interactions that are encoded in its sequence (54). There are certain requirements to a DNA construct which should provide information of nearly all its spatial movements. Primarily, it has to bear the recognition sequence of the utilized TBP. For these experiments yTBP – TBP isolated from *Saccharomyces cerevisiae* (yeast) is used. As already mentioned in chapter III.5, three-color-PIE constitutes the appropriate means to observe three dimensional dynamics. This method implies for the DNA construct, that at least three, ideally four dyes can be positioned on it in an appropriate way. Besides, the DNA segments to which the dyes are attached need to be as steady as possible so that the changes in FRET are ideally only due to conformational changes induced by TBP binding.

The DNA construct composed during this thesis is based on self-assembled DNA triple crossover complexes (TX-DNA) created by Labean *et al.* (55). Figure 31 displays a TX-DNA consisting of four ssDNA tiles.

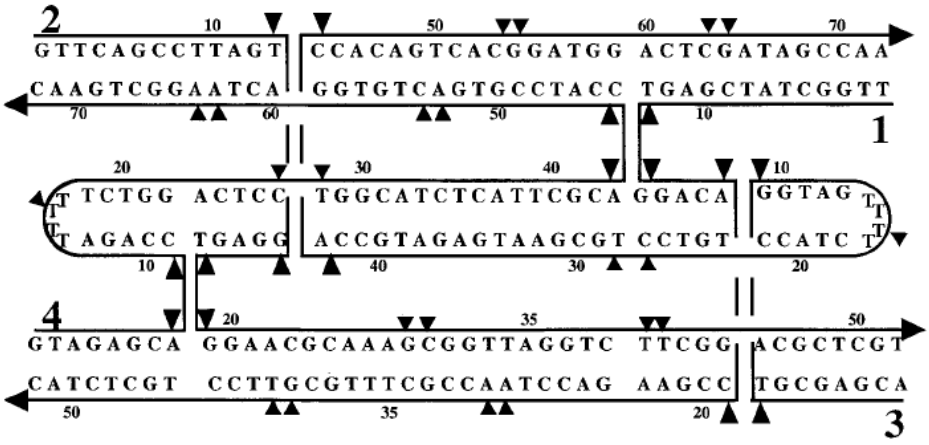

Figure 31 Self-assembled DNA triple crossover complex. Adapted from (55).

To put it in a nutshell, Labean *et al.* put all ssDNA tiles together in the same concentration. The tiles must be chosen carefully, as the base sequences decide in which form the single strands will hybridize. Thereby thymine (T) pairs with adenine (A) and guanidine (G) pairs with cytosine (C). Hybridization takes then place at temperatures above 90 °C. To ensure the strands end up in the desired formation, the hybridization solution has to be cooled down

slowly, so that the strands – when necessary – can rearrange when non-optimal base-pairing has occurred. Labean's method was chosen as a starting point for a TBP-substrate-DNA because it constitutes an efficient way to build various DNA compositions. In addition, the TX-DNA motive is planar and, thus, more "movement-resistant" than a single double helix. Sketches of the first double TX-DNA (DTX) construct on trial are shown in Figure 32.

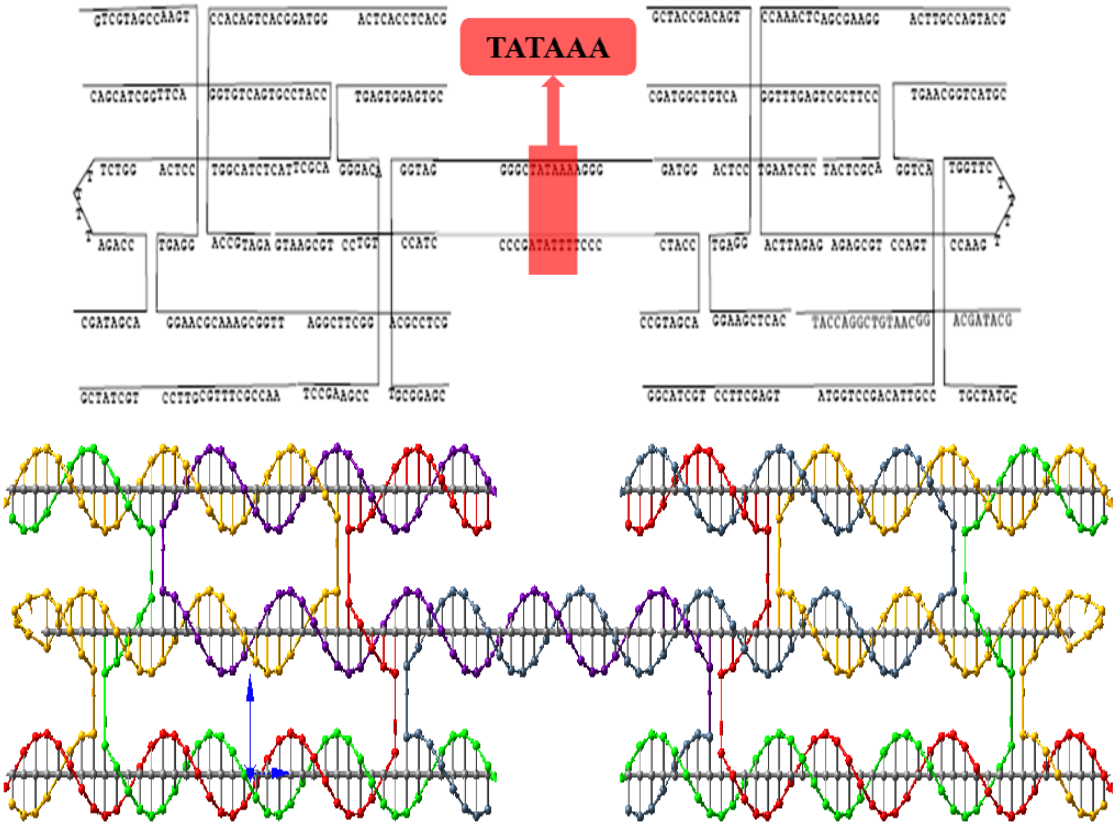

Figure 32 Sketches of the DTX-DNA construct consisting of twelve ssDNA tiles.

Altogether twelve ssDNA are used (all tiles are listed in Table 1, chapter IV.1.1). Between two TX-DNA wings lies a single dsDNA strand containing a TATAAA-sequence. The stocks solutions are brought to the same concentration by diluting them in TAE-Mg Buffer (Table 4, chapter IV.1.2). Subsequently, the equally concentrated DNA tile solutions are pipetted together in an eppendorf tube. The latter is then sealed and heated to 98°C. Cooling down takes place in a Styrofoam box over 24 h. Depending on the initial concentration of the tile solution an end concentration of the DTX-DNA construct between 400 nM (initial tile concentration 5 µM) and 8 µM (initial 100 µM) is obtained.

A Native-PAGE (see chapter IV.2) is performed to prove whether the tile assembly was successful or not. Figure 33 displays a gel containing a successfully annealed 12 tile construct

marked red. Via a DNA gel extraction (see chapter IV.3), the DNA construct could be separated from lower molecular hybridization products, also shown in Figure 33.

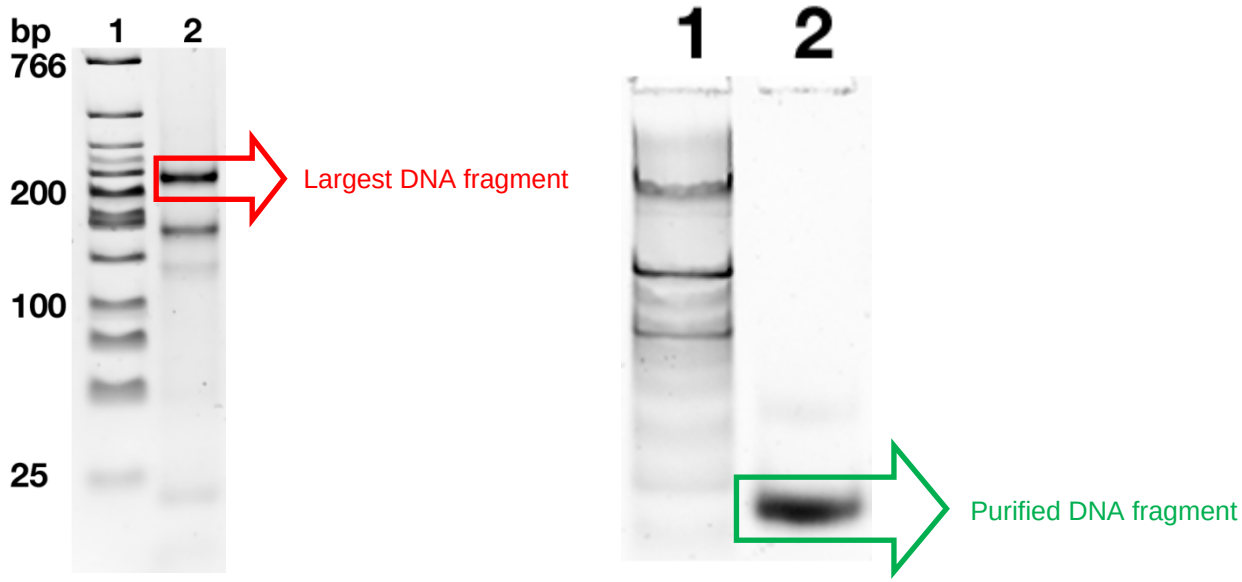

Figure 33 7.5 % Tris-HCl polyacrylamide gels with TAE-Mg buffer. Left/Right Lane 1: Low Molecular Weight Ladder; Left/Right Lane 2: 12 strand tile.

But a gel electrophoresis can just provide information about the weight of a given construct (in this case 512 bp = 338 kDa). To address whether the DTX-DNA construct has folded correctly and can be used for future PIE measurements, TBP binding to the construct's TATA box must be detected.

VI.3 Observing TBP-DNA Binding Using FCS

One possibility to observe TBP binding to DNA is fluorescence correlation spectroscopy. As already mentioned in chapter III.3, all physical parameters that give rise to fluctuations in the fluorescence signal are accessible to FCS. For example the diffusion time τ_D of a molecule through the focus. The correlation of a time series with itself, shifted by time τ, as a function of τ is called the autocorrelation function (ACF), while the so-called cross-correlation function (CCF) analyzes the similarities of two different signals. In the following chapters both analysis methods are used to monitor the binding of TBP to several DNA fragments and sequences.

VI.3.1 Autocorrelation Functions

The autocorrelation function that describes the self-similarity of a fluctuating signal can be calculated as the product of signal at a certain time *t* with the signal at the time *t*+τ. For the calculation of the ACF, freely and non-interacting species are assumed. Approximated the detection volume as three-dimensional Gaussian, the ACF is given by:

$$G_{DIFF}(\tau) = \frac{2^{-3/2}}{\langle N \rangle}\left(\frac{1}{1+\frac{4D\tau}{\omega_r^2}}\right)\left(\frac{1}{1+\frac{4D\tau}{\omega_z^2}}\right)^{1/2}$$

$\langle N \rangle$: averaged number of particles in the effective confocal volume

D: diffusion coefficient

ω_r/ω_z: radiuses of the confocal volume in x/y-plane and z-direction, defined by the Gaussian intensity distribution of the laser

One parameter in the ACF is the diffusion coefficient D, which can be derived from the Einstein-Stokes-relation.

$$D = \frac{k_B T}{6\pi\eta R_h}$$

k_B: Boltzmann constant

T: temperature

η: viscosity of the solvent

R_h: hydrodynamic radius

For non-spherical particles, D always stays in relation to ω_r, as the actual value for D is not trivially measurable. The diffusion time τ_D is then given by:

$$\tau_D = \frac{\omega_r^2}{4D}.$$

Compared to the heavy DTX-DNA construct (338 kDa), TBP is rather lightweight (30 kDa). Consequently, if the diffusion time of a labeled TBP molecule is observed it should rise noticeably if TBP binds to the DNA.

Figure 34 shows the ACF (GG1+GG2xGG1+GG2; see channels in Figure 6, chapter III.1) of Cy3 labeled yTBP (excitation ~ 550 nm; emission ~ 570 nm). The sample concentration is approximately 10 nM.

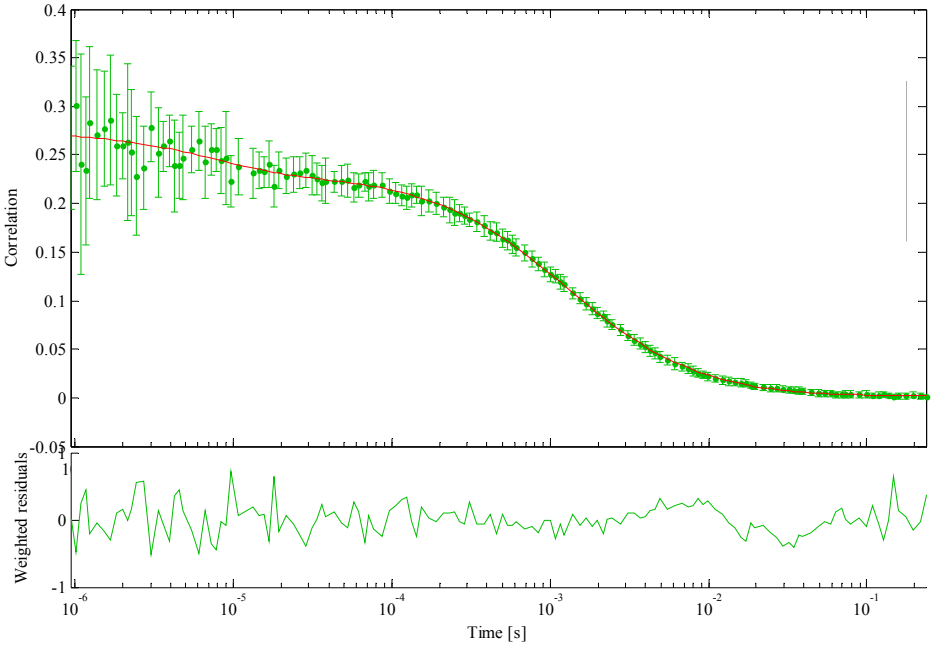

Figure 34 Autocorrelation function (green channels) of Cy3 labeled yTBP with weighted fit.

The diffusion time of yTBP is $\tau_D = 1.27 \pm 4.0 \cdot 10^{-2}$ms.

The ACF for Cy3-yTBP (GG1+GG2xGG1+GG2) in the presence of the DTX-DNA construct (incubated at RT for 30 min) is given in Figure 35.

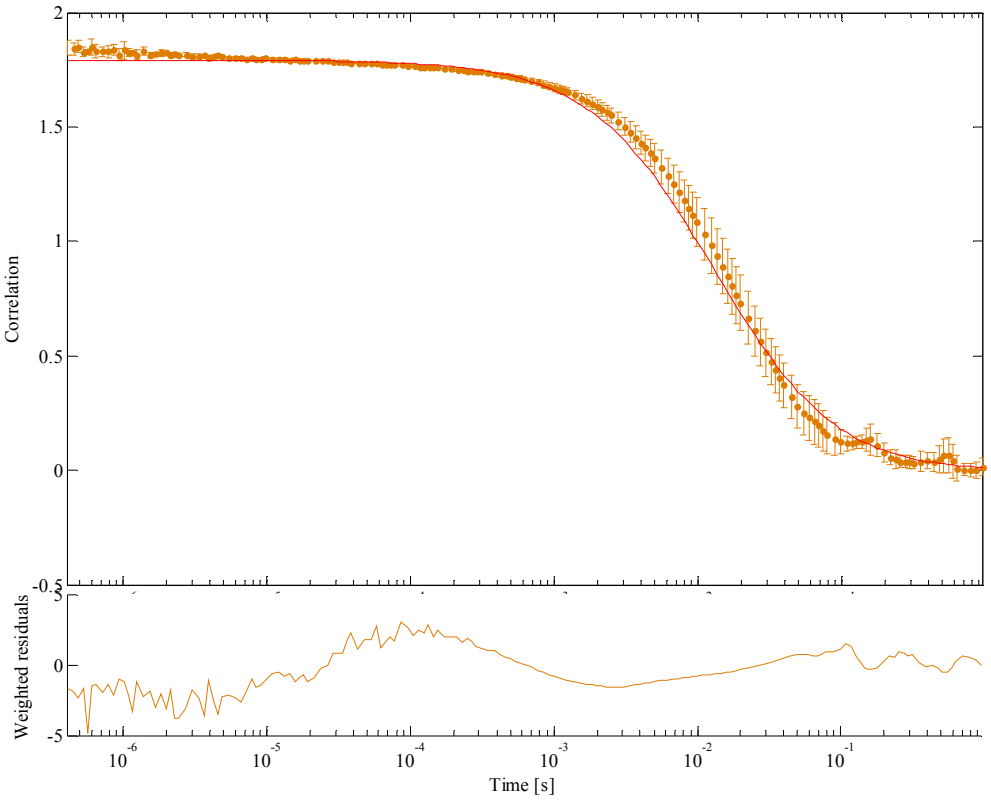

Figure 35 Normalized Autocorrelation function (green channels) of Cy3 labeled yTBP after 30 min incubation with the DTX-DNA construct.

The diffusion time of yTBP bound to the DTX DNA construct is $\tau_D = 12.8 \pm 0.9$ ms.

In order to exclude concentration changes or aggregation during the measurement, the molecular brightness of the GG1+GG2 PIE channel is plotted in comparison to the molecule number (Figure 36). While the molecule concentration (blue) stays constant, the molecular brightness (green) shows significant changes.

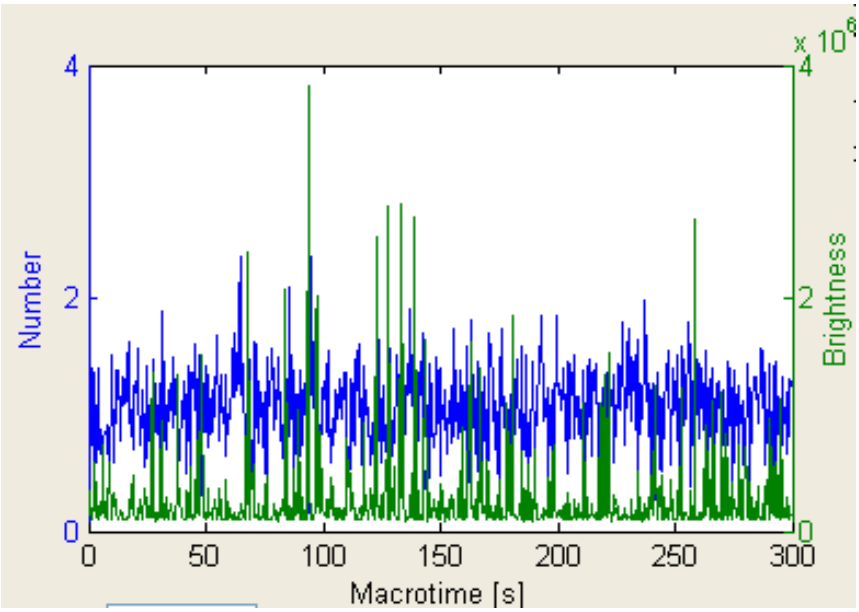

Figure 36 Molecular brightness compared to the number (i.e. concentration) of molecules the sample solution.

To have definite positive and negative controls for TBP-DNA binding, measurements with two labeled 70 bp (46 kDa) and 80 bp (53 kDa) dsDNAs were conducted (see also Table 3, chapter IV.1.1). Figure 37 and Figure 38 show the ACFs (RR1+RR2xRR1+RR2) of an Atto647N labeled mutated TATA box-DNA (mut in Table 3, chapter IV.1.1) before and after the addition of (non-labeled) yTBP (~ 10 nM).

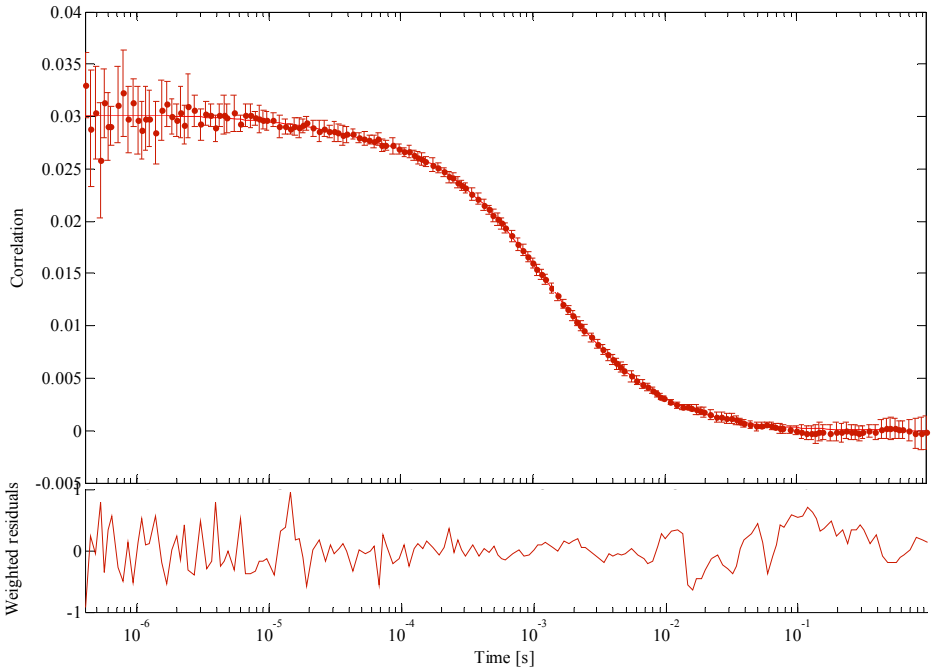

Figure 37 Autocorrelation function of 70 bp mutant TATA box-containing dsDNA labeled with Atto647N.

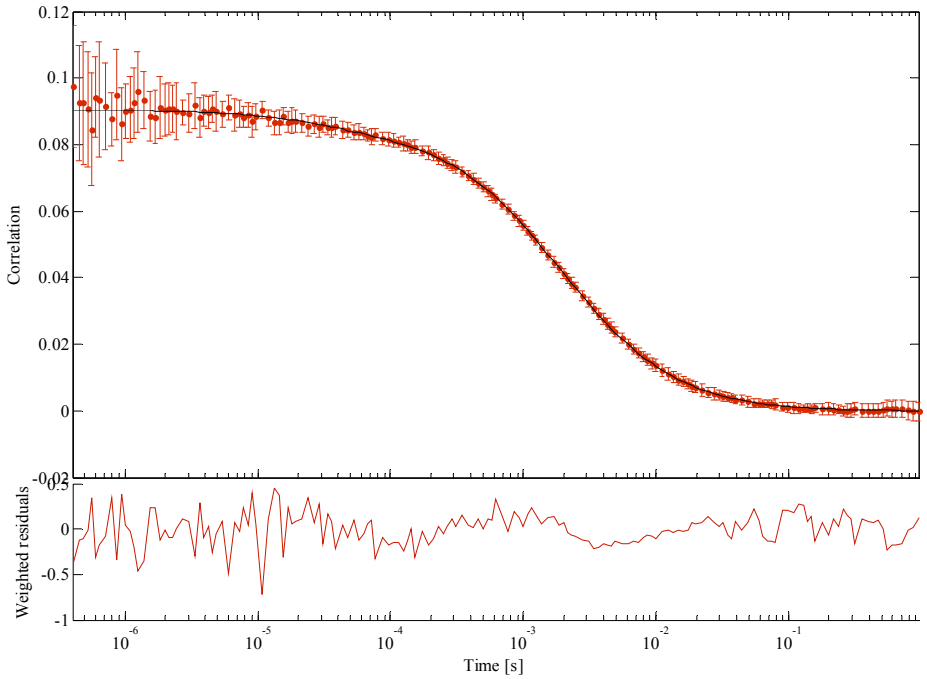

Figure 38 Autocorrelation function of 70 bp mutant TATA box-containing dsDNA labeled with Atto647N after 30 min of incubation with yTBP.

A significant increase in the diffusion time is observed due to TBP binding:

$$\tau_D(-\mathrm{TBP}) = 1.24 \pm 2.2 \cdot 10^{-2}\mathrm{ms}$$
$$\tau_D(+\mathrm{TBP}) = 1.91 \pm 2.4 \cdot 10^{-2}\mathrm{ms}$$

Hence, TBP binds also to DNA sequences apart from the TATA-motive, in this case TGTAAA. This means TBP binding does not strictly depend from a correct TATAAA-sequence.

The ACFs (GG1+GG2xGG1+GG2) of a TATA box-containing DNA segment are shown below (Figure 39 and Figure 40).

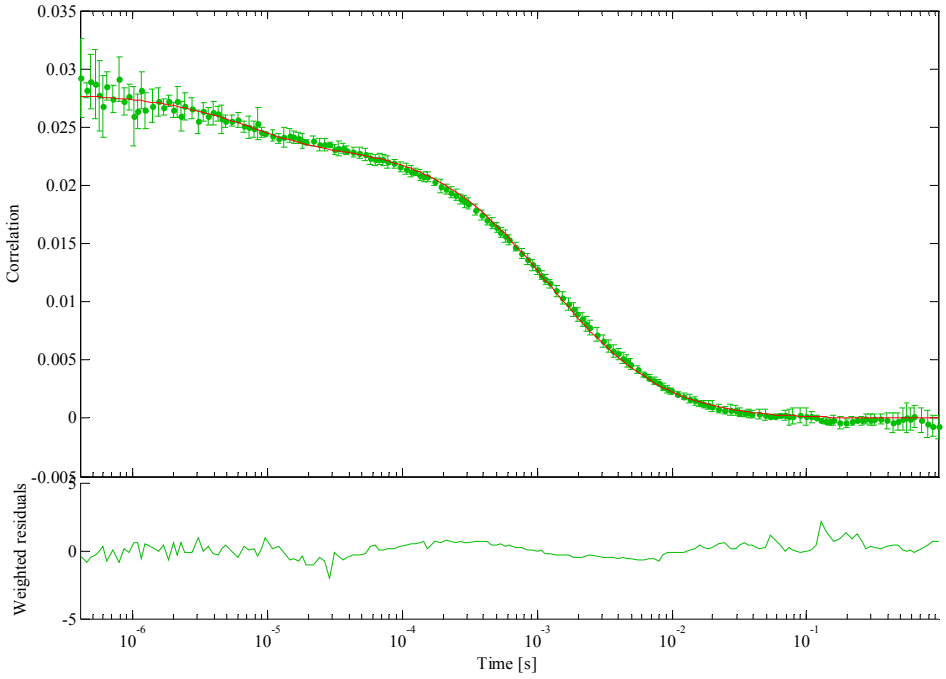

Figure 39 Autocorrelation function of 80 bp wild-type TATA box-containing dsDNA labeled with Atto532.

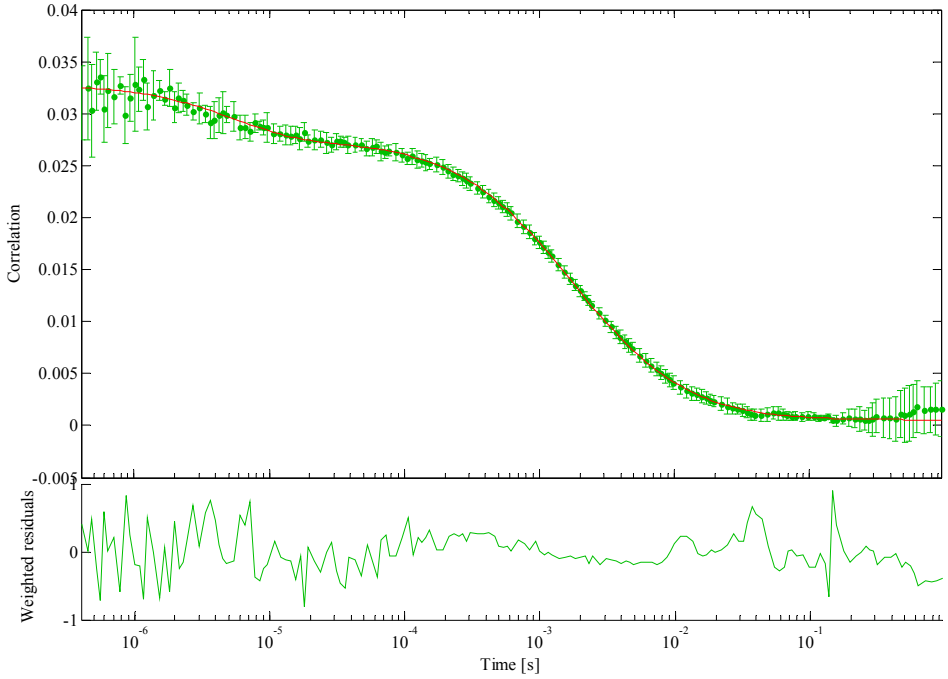

Figure 40 Autocorrelation function (green channels) of 80 bp wild-type TATA box-containing dsDNA labeled with Atto532 after 30 min of incubation with yTBP.

Although a better TBP binding is expected here, the diffusion time does not decrease significantly after yTBP-incubation in comparison to the diffusion time of the TATA box-deficient DNA.

$$\tau_D(-\text{TBP}) = 1.20 \pm 4.0 \cdot 10^{-2}\text{ms}$$
$$\tau_D(+\text{TBP}) = 1.77 \pm 2.4 \cdot 10^{-2}\text{ms}$$

In principal, an increase in the diffusion time in the resulting dimension is expected. But as the mutant-TATA box-containing DNA shows a comparable increase, a specific binding of TBP to the TATA-motive cannot be proved.

VI.3.2 Cross-correlation Functions

In order to prove the affinity of TBP to mutant TATAAA sequences, cross-correlation measurements were conducted. Theoretically, it is possible to resolve bimolecular reactions of a freely diffusing fluorophore with FCS due to the change in molecular weight and diffusion coefficient. However, the sensitivity of the ACF is limited because of the diffusion coefficient's dependency on the hydrodynamic radius. Thus, it changes with the cubed root of the molecular weight.

If two different components of the reaction are labeled with different dyes, an interaction can be detected via cross-correlating the signals of both dyes. When a double-labeled molecule (or a complex of two differently labeled molecules) passes the overlapping confocal volumes of dual-colour excitation, then a burst of photons appears in both detection channels. These two fluorescence signals are correlated. While the ACF compares a signal with itself to reveal repeating processes, the cross-correlation function (CCF) analyzes the similarities of two different signals. This method is called fluorescence cross-correlation spectroscopy (FCCS, see also chapter III.3). It is perfectly suited to investigate interactions where two components react, bind or dissolve. The CCF of channel i and j is given as

$$G(\tau)_{i\,x\,j} = \frac{\langle \delta F_i(t) \delta F_j(t+\tau) \rangle}{\langle F_i(t) \rangle \langle F_j(t) \rangle}$$

For translational diffusion, the CCFs are symmetric, so $G_{i\,x\,j}$ and $G_{j\,x\,i}$ are identical and typically averaged.

The fluorescence signals of two different species (G) and (R) can be expressed as follows, when the molecular brightness of each individual component stays constant regardless of the reaction state.

$$F_G(t) = \int W_G(\vec{r}) \cdot \varepsilon_G[C_G(\vec{r},t) + C_{GR}(\vec{r},t)]\, d\vec{r}$$

$$F_R(t) = \int W_R(\vec{r}) \cdot \varepsilon_R[C_R(\vec{r},t) + C_{GR}(\vec{r},t)]\, d\vec{r}$$

$W_G(\vec{r})$: probe volume of the ith species

$C_i(\vec{r},t)$: concentration of the ith species

$C_{GR}(\vec{r},t)$ concentration of double labeled particles

If the volumes are considered identical in size and shape and completely overlapping, the CCF is given by

$$G_{G\,x\,R}(\tau) = \frac{2^{-3/2}N_{GR}}{\langle N_G + N_{GR}\rangle\langle N_R + N_{GR}\rangle}\left(\frac{1}{1+\frac{4D_{GR}\tau}{\omega_r^2}}\right)\left(\frac{1}{1+\frac{4D_{GR}\tau}{\omega_z^2}}\right)^{1/2}$$

The CCF is indirectly proportional to the number of double-labeled particles when the total number of particles remains constant. The number of double-labeled molecules in the volume and thus the concentration $\langle C_{GR}\rangle$ can be calculated (56).

$$\langle C_{GR}\rangle = \frac{G_{G\,x\,R}(0)}{V \cdot G_G(0) \cdot G_R(0)}$$

Normally, the confocal volumes are not identical in size due to chromatic aberrations (see chapter III.2.1). This results in different diffusion times for one sample, depending on which channels are correlated, i.e. which confocal volumes are involved in the correlation.

Cross-correlation measurements were conducted with Atto532 labeled TBP (~ 6 nM) and two Atto647N labeled dsDNA fragments (~ 6 nM): one 110 bp wild-type TATA box-containing dsDNA (tb2 in Table 3, chapter IV.1.1) and a 70 bp mutant TATA box-containing dsDNA (tb1 in Table 3). The following figures display the CCFs (GG1+GG2+GR1+GR2xRR1+RR2) of both measurements and the ACFs of the cross-correlated channels (GG1+GG2+GR1+GR2xGG1+GG2+GR1+GR2 and RR1+RR2xRR1+RR2). In this case, all

photons detected after green excitation are correlated to exclude the FRET activity between the TBP- and the DNA-tagged fluorophore ($f_E \sim 40\%$, see also chapter III.5).

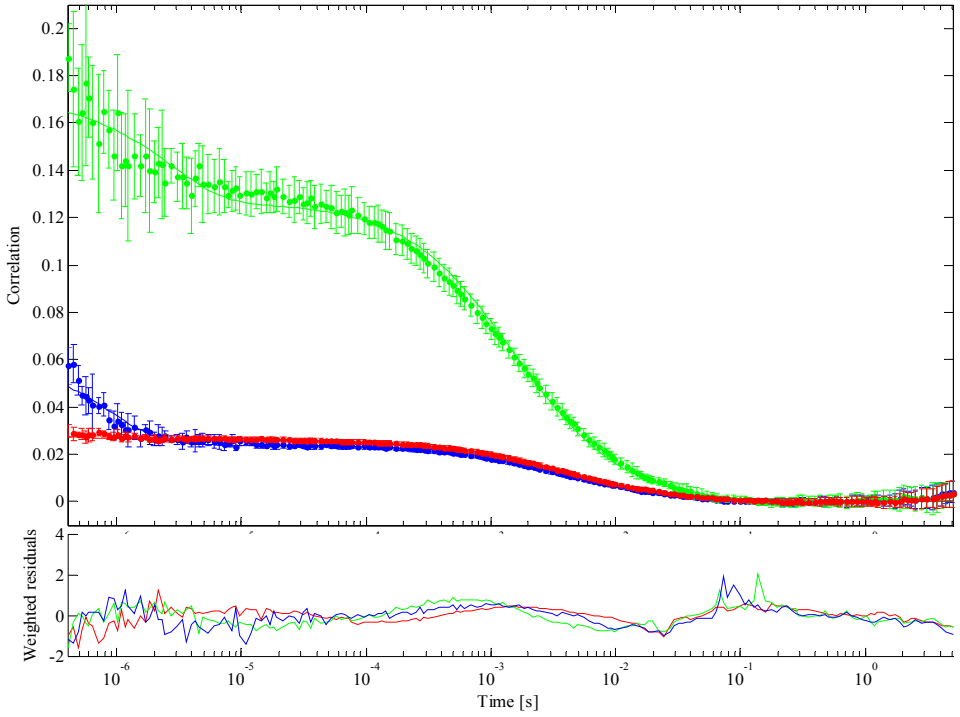

Figure 41 Correlation functions of 110 bp wild-type TATA box-containing dsDNA labeled with Atto647N after 30 min of incubation with Atto532 labeled yTBP; Green: ACF of all photons detected after green excitation; Red: ACF of red channels; Blue: CCF of both.

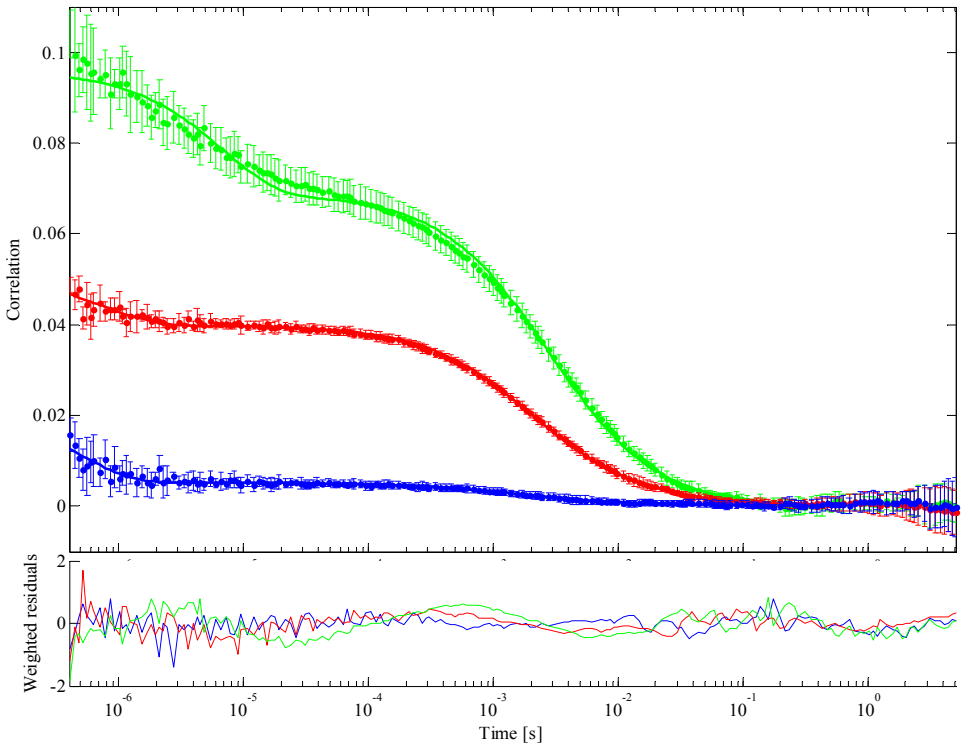

Figure 42 Correlation functions of 70 bp mutant TATA box-containing dsDNA labeled with Atto647N after 30 min of incubation with Atto532 labeled yTBP; Green: ACF of all photons detected after green excitation; Red: ACF of red channels; Blue: CCF of both.

As the diffusion times vary due to the different confocal volumes, they do not constitute the crucial parameter in these results but are still comparable to the autocorrelation measurements in chapter VI.3.1 (1.5 to 2.5 ms, depending on the length of the DNA fragment). The CCF of TBP binding to a wild-type TATA box in Figure 41 is significantly higher than the CCF of TBP binding to a mutant-type TATA box in Figure 42. This argues for more double-labeled molecules and thus bound TBP-DNA complexes. Hence, the binding efficiency of TBP to the wild-type TATA-box is higher. As the concentration of the sample components plays a role in FCCS and binding efficiency, ACFs of both cross-correlation channels are also displayed. According to these ACFs, the TBP concentration in Figures 41 and 42 (green) is lower compared to the DNA concentration (red). The fact that the DNA-TBP-ratio of the wild-type TATA box measurement is higher than that of the mutant-TATA box measurement does not affect the drawn conclusion from the comparison of the CCFs as in both cases, there is an excess of DNA. Most of the correlation functions increase for early processes on the time scale, probably due to rotational events. As the data was processed with an exponential fit, the fitting curves deviate slightly.

VI.5 Discussion

VI.5.1 Self-Assembly of a DNA Double Triple Crossover (DTX) Complex

In order to produce a DNA complex beyond the normal double helix structure, self-assembly of ssDNA tiles is highly recommendable. However, concentrating self-assembly product via standard biochemical methods like ethanol precipitation (see chapter IV.4) turns out to affect the stability of the construct. Thus, it is more efficient to start with a high initial concentration of ssDNA tiles (~ 100 µM). Theoretically, those DTX-DNA constructs can be labeled at any position, just by using labeled ssDNA tiles.

What is not clear so far, is the three dimensional movement of the complex. The connecting segment on which the TATA box is positioned constitutes the critical part. With a view to the heavy side wings, it is possible that the middle piece bends in solution. Having regard to dynamical PIE studies, high intrinsic dynamics of the DNA construct could be a limiting factor.

VI.5.2 Binding of yTBP to a DNA-DTX Complex

Two conclusions can be drawn out of the conducted FCS measurements and the resulting ACFs. In the first place, the diffusion times of the 70 bp and the 80 bp control dsDNAs (see chapter VI.3.1) show that yTBP also binds to mutant TATAAA-sequences. Both wild-type TATA box-containing and the mutant TATA box-dsDNA diffuse more slowly after incubation with the TATA box-binding protein. Nevertheless, CCFs of a TATA box-mutant dsDNA and a TATA box-containing with labeled TBP show that the affinity to the wild-type TATA box is higher. So, it is still possible that efficient TBP-binding to DNA results in a decrease of the diffusion time, due to the DNA-bending.

The second conclusion arises partly from the first one. Figure 35 points out that a DTX-DNA-yTBP solution leads to aggregates of all sizes, perceptible from the molecular brightness in Figure **36**. While the concentration of the sample stays constant, the molecular brightness shows several spikes of different heights. Initially, it seems obvious that a different amount of labeled TBP binds to each DNA complex. But the results of the cross-correlation measurements implicate that already a point mutation in the TATA box sequence leads to a decrease of TBP binding efficiency. The DTX-DNA construct does not contain TATA box variations on its wings, so excessive unspecific binding of TBP cannot explain the formation of aggregates.

Another hint for an aggregation constitutes the resulting diffusion time of 13 ms. This is significantly higher than expected as the DTX-DNA construct (338 kDa) is only 10 times heavier than TBP (30 kDa). An explanation for the apparent TBP-aggregation arises from unpublished AFM images of the purified DTX-DNA construct (conducted by Tom Sobey). They display that gel pieces remain stuck to the DNA after gel extraction and purification (see chapter IV.3). It is conceivable that several labeled TBP-molecules bind to such a remaining gel piece and thus effect the changes in molecular brightness. Besides, these gel remains could affect the diffusion time of the TBP-DTX complex. It also is possible, however, as the DTX construct cannot be considered spherical, that its wing-like shape causes the unproportional increase of the diffusion time.

In the natural cellular transcription process, many so-called transcription, factors bind directly to TBP or to the DNA at close vicinity to the TBP binding site (51). Figure 43 displays that the first transcription factor to bind is TFIIA. TFIIA binds directly to TBP and stabilizes its interaction with TATA containing DNA (57). If there are unspecific TBP-DNA interactions on the DTX-DNA construct, this stabilization could be used to get rid of them.

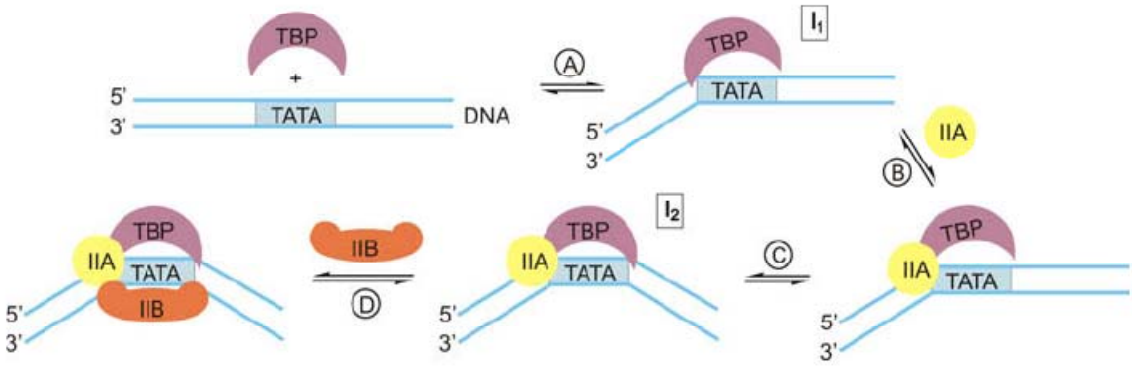

Figure 43 Suggested stepwise order of events for the binding of yTBP and transcription factors TFIIA, and TFIIB to DNA. Adapted from (52).

Furthermore, the 14 bp of the connecting segment (which are not sterically hindered) may be too short for efficient TBP binding. There are hints, that TBP needs up to 20 bp to bind properly (58). However, a DTX-DNA complex with a longer connecting strand is likely to be more flexible and the optimal conditions for the three-color FRET experiments determined.

VII Summary and Outlook

VII.1 Single Ring-GroEL Mutants

Unexpectedly, we find that the all over binding site mutant V263S of SR-EL shows a higher affinity towards DM-MBP than its wild-type form. This might be due to a new interaction revealed by the introduced mutation V263S.

Whether this affects the further folding process needs to be investigated by adding ATP and GroES. According to Fenton *et al.* (34), the residues that play a role in substrate binding are also required for binding of GroES. Figure 44 displays both polypeptide and GroES binding sites while the common ones are shown in yellow as van-der-Waals spheres. It is possible that V263S affects GroES binding as well as substrate binding.

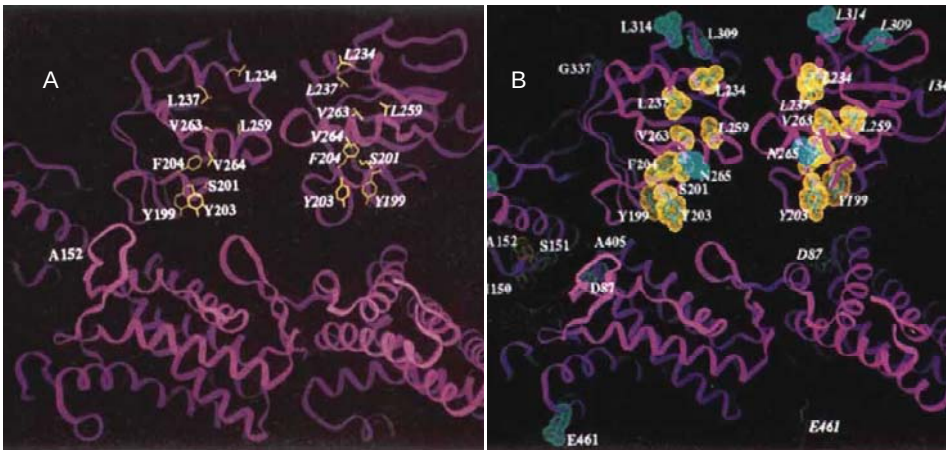

Figure 44 Residues of two 57 kDa GroEL subunits that affect substrate polypeptide binding (A) and GroES binding (B). Adapted from (34).

It is necessary to create further SR-EL mutants in order to be able to characterize single binding sites (43). A next step would be to create adequate GroEL mutants. Other DM-MBP mutants can lead to information about potential binding residues on the substrate protein itself. Labeling of both GroEL and MBP might also help to monitor binding and folding behaviour.

Eventually, it will be necessary to characterize discrete steps during the folding process, i.e. not only initial and final folding state but also the intermediate states. Therefore, dynamic measurements need to be performed in addition to equilibrium measurements. As already mentioned in chapter V.4, a coaxial mixing device enables exactly this approach.

VII.2 DNA-TBP Binding and Three-Color-PIE

We were able to find a promising precursor for observing dynamical changes in DNA upon interaction with TBP. The original idea is to attach three dyes to this construct and perform three color-PIE measurements (see chapter III.4). Figure 45 shows a draft of the DTX-DNA construct labeled with the according dyes for the given three-color-PIE setup (Atto488, Alexa568, Atto700).

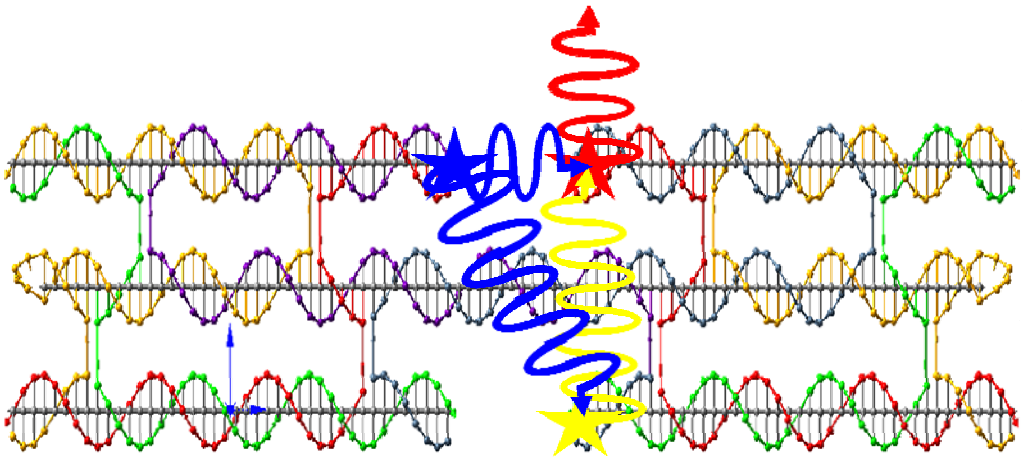

Figure 45 Sketch of a three-dye labeled DTX-DNA construct.

Prior to completion of these studies, the TBP-DNA interaction has to be TATA box specific. Although we found that yTBP binds quite specifically to the TATAAA sequence, unspecific binding to the side-wings of the construct cannot be completely excluded. One approach is to add a transcription factor to the reaction solution, in our case that would be TFIIA, to stabilize the TBP-TATA box interaction. How well this works for the given construct can be investigated using FCS/FCCS or by an electrophoretic mobility shift assay (EMSA). A possible protocol for a TBP-DNA EMSA can be found in Xie *et al.* (59) and Gilfillan *et al.* (60). In order to get rid of the remaining gel pieces stuck to the DTX-DNA construct, new purification techniques must be tried out like filtering the diluted DNA construct samples.

Another issue which needs to be addressed is the length of the binding site. It is conceivable that steric hindrances with the DTX-DNA are possible, inhibiting protein binding. In addition, DNase assays performed by Darst *et al*. showed that binding of TBP led to protection from DNase I digestion of ~20 bp of DNA centered on the TATA box (58). These results implicate that sterically speaking, TBP needs more than the current 24 bp middle dsDNA piece, as only 14 bp are not sterically shielded by the TX-wings. Elongation of this dsDNA strand could lead to destabilization of the basal DTX-DNA movements. Although DNA should be stable up to a length of 50 bp (61) – depending on the salt concentration – it is not possible to predict

the influence of the TX-wings. This question could be solved by FCCS and spFRET measurements of DTX-DNA constructs with connection segments of various lengths, labeled as shown in Figure 46.

Figure 46 Draft of possible dye positions on the DTX-DNA construct to measure basal dynamics.

FCS measurements could possibly reveal conformational dynamics by fluctuations in FRET, depending on which timescale they occur. By using two different labeling models, more intramolecular distances are measurable. Thus, conformational modes such as twisting or bending of the DNA are detectable.

In case the DTX-DNA construct turns out to be too unstable in its movements, there are other options to design an appropriate DNA model, e.g. DNA Origami. This “one-pot method” uses a few hundred short DNA strands to staple a very long strand into two-dimensional structures that adopt any desired shape (62). These constructs may be even more stable and hence more insusceptible to intrinsic movements than the DTX construct.

VIII Abbreviations

AFM	Atomic force microscopy
ACF	Autocorrelation function
APD	Avalanche photodiode
APS	Ammoniumperoxodisulfate
ATP	Adenosine triphosphate
CCF	Cross-correlation function
dsDNA	Double-stranded DNA
DTT	Dithiothreitol
EDTA	Ethylenediaminetetraacetic acid
FCS	Fluorescence correlation spectroscopy
FRET	Förster/Fluorescence resonance energy transfer
MPF	Multi-parameter fluorescence
NP40	Nonylphenoxylpolyethoxylethanol
PAGE	Polyacrylamide gel electrophoresis
PBS	Polarizing beam splitter cube
PIE	Pulsed interleaved excitation
PMSF	Phenylmethylsulphonyl fluoride
RT	Room temperature
ssDNA	Single-stranded DNA
TCSPC	Time correlated single photon counting
TEMED	N,N,N',N'-Tetramethylethylenediamine
TFIIA	Transcription factor II A
yTBP	TATA box-binding protein from yeast

IX References

1. Avery, O. T., C. M. Macleod, and M. McCarty. 1944. Studies on the Chemical Nature of the Substance Inducing Transformation of Pneumococcal Types : Induction of Transformation by a Desoxyribonucleic Acid Fraction Isolated from Pneumococcus Type Iii. J Exp Med 79:137-158.

2. Watson, J. D., and F. H. Crick. 1953. Genetical implications of the structure of deoxyribonucleic acid. Nature 171:964-967.

3. Ormo, M., A. B. Cubitt, K. Kallio, L. A. Gross, R. Y. Tsien, and S. J. Remington. 1996. Crystal structure of the Aequorea victoria green fluorescent protein. Science 273:1392-1395.

4. Heimstädt, O. 1911. Das Fluoreszenzmikroskop. Z. Wiss. Mikrosk. 28: 330-337.

5. Ellinger, P. H., A. 1929. Mikroskopische Beobachtungen an lebenden Organen mit Demonstrationen (Intravitalmikroskopie). Arch. Exp. Pathol. Phar. 147:63.

6. Ploem, J. S. 1967. The use of a vertical illuminator with interchangeable dichroic mirrors for fluorescence microscopy with incidental light. Z Wiss Mikrosk 68:129-142.

7. Minsky, M. 1961. Microscopy Apparatus. USA.

8. Spector, D. L., editor. 2006. Basic Methods in Microscopy. Cold Spring Harbor Laboratory Press, Cold Spring Harbor.

9. van Meer, G., E. H. Stelzer, R. W. Wijnaendts-van-Resandt, and K. Simons. 1987. Sorting of sphingolipids in epithelial (Madin-Darby canine kidney) cells. J Cell Biol 105:1623-1635.

10. White, J. G., W. B. Amos, and M. Fordham. 1987. An evaluation of confocal versus conventional imaging of biological structures by fluorescence light microscopy. J Cell Biol 105:41-48.

11. Betzig, E., and R. J. Chichester. 1993. Single Molecules Observed by Near-Field Scanning Optical Microscopy. Science 262:1422-1425.

12. Lu, H. P., L. Xun, and X. S. Xie. 1998. Single-molecule enzymatic dynamics. Science 282:1877-1882.

13. Förster, T. 1946. Energiewanderung und Fluoreszenz. Naturwissenschaften 6:166-175.

14. Stryer, L., and R. P. Haugland. 1967. Energy transfer: a spectroscopic ruler. Proc Natl Acad Sci U S A 58:719-726.

15. Bacskai, B. J., B. Hochner, M. Mahaut-Smith, S. R. Adams, B. K. Kaang, E. R. Kandel, and R. Y. Tsien. 1993. Spatially resolved dynamics of cAMP and protein kinase A subunits in Aplysia sensory neurons. Science 260:222-226.

16. Gadella, T. W., Jr., and T. M. Jovin. 1995. Oligomerization of epidermal growth factor receptors on A431 cells studied by time-resolved fluorescence imaging microscopy. A stereochemical model for tyrosine kinase receptor activation. J Cell Biol 129:1543-1558.

17. Müller, B. K. 2006. Die gepulste alternierende Anregung in der konfokalen Fluoreszenzspektroskopie: Entwicklung und Anwendungen. In Fakultät für Chemie und Pharmazie. Ludwig-Maximilians-Universität München.

18. Naredi-Rainer, N. 2009. Multi Parameter Fluorescence Spectroscopy -Setup, Assembly and Applications. Ludwig-Maximilians-Universität München.

19. Patterson, G. H., D. W. Piston, and B. G. Barisas. 2000. Forster distances between green fluorescent protein pairs. Anal Biochem 284:438-440.

20. Clegg, R. M. 1996. Fluorescence Resonance Energy Transfer, Fluorescence Imaging. John Wiley & Sons, New York.

21. Lakowicz, J. R. 1988. Principles of frequency-domain fluorescence spectroscopy and applications to cell membranes. Subcell Biochem 13:89-126.

22. dos Remedios, C. G., and P. D. Moens. 1995. Fluorescence resonance energy transfer spectroscopy is a reliable "ruler" for measuring structural changes in proteins. Dispelling the problem of the unknown orientation factor. J Struct Biol 115:175-185.

23. Day, R. N., A. Periasamy, and F. Schaufele. 2001. Fluorescence resonance energy transfer microscopy of localized protein interactions in the living cell nucleus. Methods 25:4-18.

24. Muller, C. B., A. Loman, V. Pacheco, F. Koberling, D. Willbold, W. Richtering, and J. Enderlein. 2008. Precise measurement of diffusion by multi-color dual-focus fluorescence correlation spectroscopy. EPL (Europhysics Letters) 83:46001.

25. Elson E.L., M. D. 1974. Fluorescence Correlation Spectroscopy I: Conceptual Basis and Theory. Biopolymers 13.

26. Dertinger, T., V. Pacheco, I. von der Hocht, R. Hartmann, I. Gregor, and J. Enderlein. 2007. Two-focus fluorescence correlation spectroscopy: a new tool for accurate and absolute diffusion measurements. Chemphyschem 8:433-443.

27. Magde, D., E. L. Elson, and W. W. Webb. 1974. Fluorescence correlation spectroscopy. II. An experimental realization. Biopolymers 13:29-61.

28. Schwille, P. Fluorescence Correlation Spectroscopy.

29. Hohng, S., C. Joo, and T. Ha. 2004. Single-molecule three-color FRET. Biophys J 87:1328-1337.

30. Frydman, J. 2001. Folding of newly translated proteins in vivo: the role of molecular chaperones. Annu Rev Biochem 70:603-647.

31. Hartl, F. U., and M. Hayer-Hartl. 2009. Converging concepts of protein folding in vitro and in vivo. Nat Struct Mol Biol 16:574-581.

32. Sharma, S., K. Chakraborty, B. K. Muller, N. Astola, Y. C. Tang, D. C. Lamb, M. Hayer-Hartl, and F. U. Hartl. 2008. Monitoring protein conformation along the pathway of chaperonin-assisted folding. Cell 133:142-153.

33. Jewett, A. I., and J. E. Shea. 2009. Reconciling theories of chaperonin accelerated folding with experimental evidence. Cell Mol Life Sci.

34. Fenton, W. A., Y. Kashi, K. Furtak, and A. L. Horwich. 1994. Residues in chaperonin GroEL required for polypeptide binding and release. Nature 371:614-619.

35. Braig, K., Z. Otwinowski, R. Hegde, D. C. Boisvert, A. Joachimiak, A. L. Horwich, and P. B. Sigler. 1994. The crystal structure of the bacterial chaperonin GroEL at 2.8 A. Nature 371:578-586.

36. Saibil, H. R., and N. A. Ranson. 2002. The chaperonin folding machine. Trends Biochem Sci 27:627-632.

37. Landry, S. J., J. Zeilstra-Ryalls, O. Fayet, C. Georgopoulos, and L. M. Gierasch. 1993. Characterization of a functionally important mobile domain of GroES. Nature 364:255-258.

38. Xu, Z., A. L. Horwich, and P. B. Sigler. 1997. The crystal structure of the asymmetric GroEL-GroES-(ADP)7 chaperonin complex. Nature 388:741-750.

39. Tang, Y. C., H. C. Chang, A. Roeben, D. Wischnewski, N. Wischnewski, M. J. Kerner, F. U. Hartl, and M. Hayer-Hartl. 2006. Structural features of the GroEL-GroES nano-cage required for rapid folding of encapsulated protein. Cell 125:903-914.

40. Chun, S. Y., S. Strobel, P. Bassford, Jr., and L. L. Randall. 1993. Folding of maltose-binding protein. Evidence for the identity of the rate-determining step in vivo and in vitro. J Biol Chem 268:20855-20862.

41. Sparrer, H., K. Rutkat, and J. Buchner. 1997. Catalysis of protein folding by symmetric chaperone complexes. Proc Natl Acad Sci U S A 94:1096-1100.

42. Wang, J. D., M. D. Michelitsch, and J. S. Weissman. 1998. GroEL-GroES-mediated protein folding requires an intact central cavity. Proc Natl Acad Sci U S A 95:12163-12168.

43. Farr, G. W., K. Furtak, M. B. Rowland, N. A. Ranson, H. R. Saibil, T. Kirchhausen, and A. L. Horwich. 2000. Multivalent binding of nonnative substrate proteins by the chaperonin GroEL. Cell 100:561-573.

44. Rye, H. S., A. M. Roseman, S. Chen, K. Furtak, W. A. Fenton, H. R. Saibil, and A. L. Horwich. 1999. GroEL-GroES cycling: ATP and nonnative polypeptide direct alternation of folding-active rings. Cell 97:325-338.

45. Liu, H., E. Kovacs, and P. A. Lund. 2009. Characterisation of mutations in GroES that allow GroEL to function as a single ring. FEBS Lett 583:2365-2371.

46. Hamadani, K. M., and S. Weiss. 2008. Nonequilibrium single molecule protein folding in a coaxial mixer. Biophys J 95:352-365.

47. Stryer, L. 2003. Biochemie. Spektrum Akademischer Verlag, Heidelberg.

48. White, R. J., S. P. Jackson, and P. W. Rigby. 1992. A role for the TATA-box-binding protein component of the transcription factor IID complex as a general RNA polymerase III transcription factor. Proc Natl Acad Sci U S A 89:1949-1953.

49. Kim, Y., J. H. Geiger, S. Hahn, and P. B. Sigler. 1993. Crystal structure of a yeast TBP/TATA-box complex. Nature 365:512-520.

50. van Werven, F. J., H. A. van Teeffelen, F. C. Holstege, and H. T. Timmers. 2009. Distinct promoter dynamics of the basal transcription factor TBP across the yeast genome. Nat Struct Mol Biol 16:1043-1048.

51. Tolic-Norrelykke, S. F., M. B. Rasmussen, F. S. Pavone, K. Berg-Sorensen, and L. B. Oddershede. 2006. Stepwise bending of DNA by a single TATA-box binding protein. Biophys J 90:3694-3703.

52. Schlüsche, P. 2007. Untersuchung der Funktion und Dynamik von DNA-Transkriptionsfaktoren mittels Einzelmolekül-Fluoreszenzmikroskopie. Ludwig-Maximilians-Universität München.

53. Schluesche, P., G. Stelzer, E. Piaia, D. C. Lamb, and M. Meisterernst. 2007. NC2 mobilizes TBP on core promoter TATA boxes. Nat Struct Mol Biol 14:1196-1201.

54. Kukolka, F., B. K. Muller, S. Paternoster, A. Arndt, C. M. Niemeyer, C. Brauchle, and D. C. Lamb. 2006. A single-molecule Forster resonance energy transfer analysis of fluorescent DNA-protein conjugates for nanobiotechnology. Small 2:1083-1089.

55. Labean, T. H., Yan, H., Kopatsch, J., Liu F., Winfree, E., Reif, J. H., Seeman, N. C. 2000. Construction, Analysis, Ligation, and Self-Assembly of DNA Triple Crossover Complexes. J Am Chem Soc 122:1848-1860

56. Schwille, P., F. J. Meyer-Almes, and R. Rigler. 1997. Dual-color fluorescence cross-correlation spectroscopy for multicomponent diffusional analysis in solution. Biophys J 72:1878-1886.

57. Ozer, J., K. Mitsouras, D. Zerby, M. Carey, and P. M. Lieberman. 1998. Transcription factor IIA derepresses TATA-binding protein (TBP)-associated factor inhibition of TBP-DNA binding. J Biol Chem 273:14293-14300.

58. Darst, R. P., D. Wang, and D. T. Auble. 2001. MOT1-catalyzed TBP-DNA disruption: uncoupling DNA conformational change and role of upstream DNA. EMBO J 20:2028-2040.

59. Xie, J., M. Collart, M. Lemaire, G. Stelzer, and M. Meisterernst. 2000. A single point mutation in TFIIA suppresses NC2 requirement in vivo. EMBO J 19:672-682.

60. Gilfillan, S., G. Stelzer, E. Piaia, M. G. Hofmann, and M. Meisterernst. 2005. Efficient binding of NC2.TATA-binding protein to DNA in the absence of TATA. J Biol Chem 280:6222-6230.

61. Strick, T., J. Allemand, V. Croquette, and D. Bensimon. 2000. Twisting and stretching single DNA molecules. Prog Biophys Mol Biol 74:115-140.

62. Rothemund, P. W. 2006. Folding DNA to create nanoscale shapes and patterns. Nature 440:297-302.